Rational Design Strategy of Multicomponent Si/FeSeO$_x$@N-Doped Graphitic Carbon Hybrid Microspheres Intertwined with N-Doped Carbon Nanotubes as Anodes for Ultra-Stable Lithium-Ion Batteries

Jae Seob Lee, Jung Yeon Kim, Hyun Seon Ahn, Hye Seon Ka, Rakesh Saroha, Do Won Jeong, Yun Chan Kang, Dong-Won Kang,* and Jung Sang Cho*

Herein, an efficient synthesis approach is introduced for the fabrication of a hybrid anode consisting of porous microspheres with biphasic silicon (Si)-amorphous iron selenite (Si/FeSeO$_x$) nanocrystals enveloped within an N-doped graphitic carbon (NGC) matrix and encased by well-grown, highly intertwined N-doped carbon nanotubes (CNTs) (Si/FeSeO$_x$@NGC/N-CNT). Si and FeSeO$_x$ serve as the active components, contributing to the overall discharge capacity of the hybrid anode. Additionally, FeSeO$_x$ not only enhances the structural integrity of the nanostructure by channelizing the drastic volume variation of Si, but also expedites the diffusion of lithium ions, thereby promoting kinetically favored redox reactions. The NGC matrix serves as the primary pathway for efficient electron transfer within the electrode, whereas the well-grown N-CNTs network acts as a secondary pathway for subsequent electron transfer to the current collector. The porous structure achieved via selective removal of amorphous carbon ensures the smooth diffusion of charged species by shortening the effective charge diffusion length and accommodating the substantial volume changes during cycling. Correspondingly, the Si/FeSeO$_x$@NGC/N-CNT anodes demonstrate significant enhancements in electrochemical performance, including one-order higher diffusion coefficients ($\approx 10^{-12}$ cm^2 s^{-1}), exceptional rate capability (till 30 A g^{-1}), and extraordinary cycling stability at 0.5, 1.0, and 3.0 A g^{-1}.

1. Introduction

Silicon (Si) has recently garnered significant attention as a potential replacement for conventional graphite anodes owing to its impressive gravimetric capacity (4200 mAh g^{-1}) and volumetric capacity (2400 mAh cm^{-3}) when utilized at low discharge potentials.[1–3] The key to the high discharge capacity of Si is its unique chemical properties. Si can form bonds with up to four lithium (Li) atoms, leading to the creation of a Li$_{4.4}$Si/Li$_{22}$Si$_5$ alloy, whereas graphite can only bond one Li atom to six carbon (C) atoms (LiC$_6$).[4,5] Furthermore, Si possesses a lower discharge potential of $\approx$0.2 V versus Li/Li$^+$, cost-effectiveness, natural abundance, and eco-friendliness.[6] Despite its promising attributes, the widespread adoption of Si as an anode material presents significant challenges, primarily due to its densely packed crystal structure, which results in substantial volume expansion ($\approx$400%) during the charge–discharge processes.[7] This expansion can have detrimental effects, including pulverization and

J. S. Lee, J. Y. Kim, H. S. Ahn, H. S. Ka, R. Saroha, D. W. Jeong, J. S. Cho
Department of Engineering Chemistry
Chungbuk National University
Chungbuk 28644, Republic of Korea
E-mail: jscho@cbnu.ac.kr

J. S. Lee, Y. C. Kang
Department of Materials Science and Engineering
Korea University
Anam-Dong, Seongbuk-Gu, Seoul 02841, Republic of Korea

R. Saroha
Department of Materials Science and Engineering
Ajou University
206 Worldcup-ro, Yeongtong-gu, Suwon-si 16499, Republic of Korea

D.-W. Kang
School of Energy Systems Engineering
Chung-Ang University
Seoul 06974, Republic of Korea
E-mail: kangdwn@cau.ac.kr

J. S. Cho
Biomedical Research Institute
Chungbuk National University Hospital
Chungbuk 28644, Republic of Korea

J. S. Cho
Advanced Energy Research Institute
Chungbuk National University
Cheongju 28644, Chungbuk, Republic of Korea

amorphization of the active Si material within an electrode. Consequently, the active material is lost, and the battery undergoes capacity degradation over time. Another complication arises from the formation of a continuously grown thick solid electrolyte interphase (SEI) due to electrolyte decomposition at low potentials.[8] This diminishes the electrochemical activity of the electrode, which further impairs the cycling performance and overall lifespan of the battery.

To overcome these challenges, researchers have been actively exploring several nanostructure design strategies which encompass a range of innovative approaches, including the development of Si composites M_xSi_y (where M represents elements like Mg, Ni, Fe, Co, Ca, and x or y can take values of 1 or 2),[9–11] dispersion of Si nanoparticles within highly conductive architectures like reduced graphene oxide,[12,13] creation of hollow or yolk-shell nanostructures to accommodate significant volume expansion of Si,[14–16] and binder modification,[17,18] among other methods.[7,19,20] Transition metal oxides (TMOs), denoted as M_xO_y (where M represents a transition metal), have also been rigorously assessed as advanced anode materials for lithium-ion batteries (LIBs).[21–23] Unlike Si, TMOs do not form alloys with Li metal; instead, they establish a metallic network that offers multielectron transmission per transition metal during the conversion process (TMOs → TM^0).[24] This characteristic results in high theoretical discharge capacities with minimal volume fluctuations (<100%); a marked improvement over alloy-type materials (>300%).[25] Consequently, the integration of high-capacity Si with low-capacity TMOs in a hybrid composite is a facile strategy for achieving a stable and long-lasting advanced anode. In such hybrid composites, both components contribute to the attainment of high discharge capacities (depending on the voltage window), whereas the TMO component plays a crucial role in stabilizing the SEI film and synergistically improving the overall electrochemical properties. For instance, Wang et al. prepared Fe_2O_3/C-modified Si nanoparticles, which delivered a high discharge capacity at low current density (2942 mAh g^{-1} at 100 mA g^{-1}), good rate capability (423 mAh g^{-1} at 10 A g^{-1}), and stable cycling performance (680 mAh g^{-1} at 1.0 A g^{-1} after 300 cycles).[26] Despite these promising outcomes, several challenges remain. For instance, the low electronic conductivities of both Si and TMO, as well as their composites, need to be carefully considered to achieve further improvements in the rate capability and cycling performance. Additionally, controlling the crystal growth in TMO during the synthesis process is another critical aspect that requires focused attention in the quest for advanced LIB anodes.

Metal selenite nanostructures, which form heterostructures encompassing both metal oxide and selenide phases, have demonstrated remarkable properties including high electronic conductivities and superior redox reaction capabilities.[27,28] Moreover, the built-in electric fields at different types of heterointerfaces present within the heterostructure resulted in better acceleration of charge transport. For instance, Kang et al. reported the synthesis of binary metal (Ni, Co) selenite (($NiCo$)SeO_3) as a LIB anode with an enhanced cycling performance (680 mAh g^{-1} at 5.0 A g^{-1} after 1500 cycles).[28] Likewise, Liu et al. also synthesized hierarchical $CoSeO_3 \cdot 2H_2O$ nanoflowers, which show a discharge capacity of 626 mAh g^{-1} at 0.5 A g^{-1} after 180 cycles. This unsatisfactory cycling performance was mainly due to

uncontrolled crystal growth.[29] However, there have been no reports on the development of a hybrid porous conductive anode that combines Si owing to its high-capacity properties, an amorphous selenite phase to enhance structural integrity, and a highly conductive framework to bolster the overall conductivity.

Based on the above discussion, we introduce an efficient synthesis approach for crafting sophisticated multicomponent anode materials. This material consists of porous microspheres comprising a biphasic silicon-amorphous iron selenite ($Si/FeSeO_x$) phase enveloped within an N-doped graphitic carbon (NGC) matrix, which also incorporates well-grown, highly intertwined N-doped carbon nanotubes (CNTs) (denoted as $Si/FeSeO_x$@NGC/N-CNT). Depending on the voltage window range, both the $FeSeO_x$ and Si nanoparticles contribute to the overall discharge capacity of the composite material. The $FeSeO_x$ nanoparticles improve the structural integrity of the nanostructures via effective volume channelization of Si through the different lithiation/delithiation voltage range, and facilitate rapid Li-ion diffusion, thereby promoting kinetically favored redox reactions. Additionally, to further enhance the overall conductivity and charge transfer characteristics of Si-based nanostructures, in-depth optimization is performed to the formation of NGC matrix and well-grown N-CNT networks. The NGC matrix surrounding $Si/FeSeO_x$ nanocrystals serves as the primary pathway for efficient and fast electron transfer. Notably, N-CNT networks act as a secondary pathway between the structures improving diffusion kinetics in the hybrid nanostructure, and maintaining the electrical contact by preventing the fragments of the compromised structure from completely detaching in the microsphere. The porosity of the composite nanostructures was introduced through the selective removal of amorphous carbon (AC) species. It facilitates smooth diffusion of charged species by shortening the effective charge diffusion length and accommodates severe volume changes during the lithiation/delithiation processes.

Benefitted from the rational nanostructural strategy introduced in this study, the hybrid multicomponent $Si/FeSeO_x$@NGC/N-CNT anodes have exhibited a significant enhancement in the overall electrochemical performance, such as high-rate capability (up to 30 A g^{-1}) and long-term cycling stability at low and high current densities (0.5, 1.0, and 3.0 A g^{-1}). As a result of these remarkable structural and electrochemical advancements, we firmly believe that our findings will serve as a cornerstone for the development of highly conductive and multicomponent hybrid anode materials to find application in a diverse range of energy storage and beyond.

2. Results and Discussion

The porous microspheres comprising biphasic silicon-amorphous iron selenite ($Si/FeSeO_x$) nanocrystals enveloped within an NGC matrix with well-grown and highly intertwined N-CNTs ($Si/FeSeO_x$@NGC/N-CNT) were prepared using a facile spray pyrolysis technique and multistep heat treatment. The detailed formation mechanism of the $Si/FeSeO_x$@NGC/N-CNT microspheres is shown in **Scheme 1**. The precursor colloidal solution consisting of Si nanopowders, Fe nitrate, and PVP was uniformly dropletized by the ultrasonic nebulizer (Scheme 1-①). Fe nitrate served as the Fe precursor for the
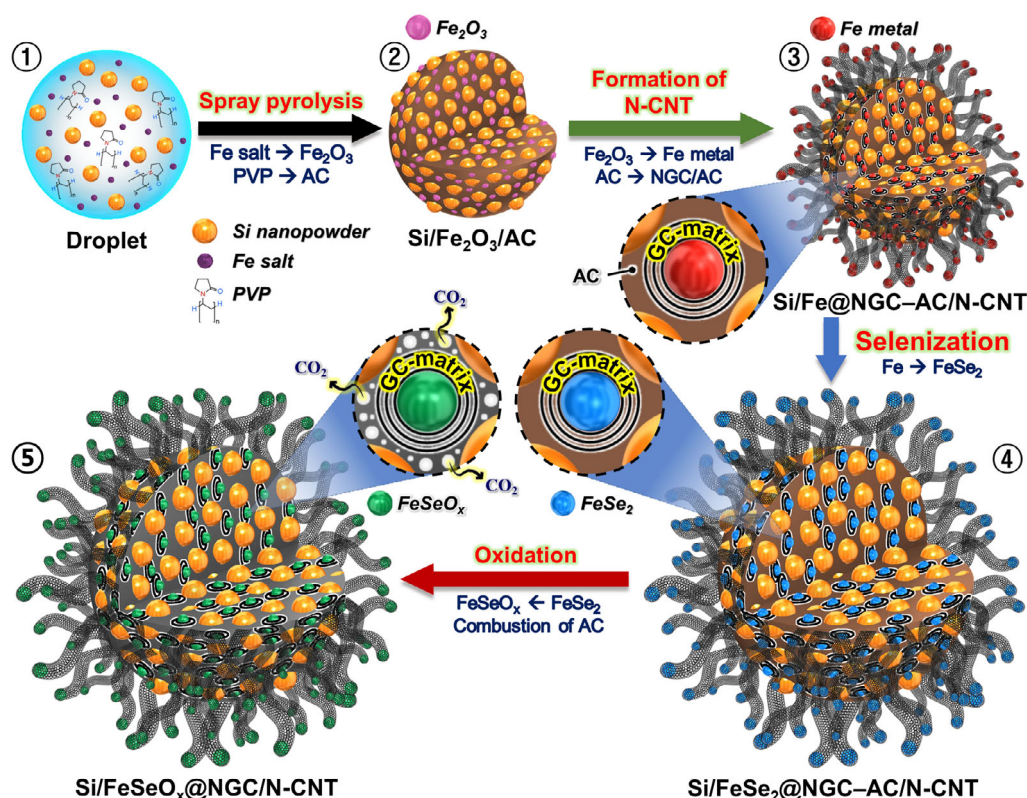
Scheme 1. Schematic representation of the formation mechanism (①–⑤) of the porous microspheres comprising a biphasic silicon-amorphous iron selenite (Si/FeSeO$_x$) nanocrystals enveloped within an NGC matrix with well-grown and highly intertwined N-CNTs (referred to as Si/FeSeO$_x$@NGC/N-CNT).

formation of the FeSeO$_x$ phase, whereas amphiphilic PVP simultaneously served as a carbon source to form the NGC matrix and as a surface functionalizer for the Si nanopowders. This PVP-induced functionalization ensured uniform dispersion of Si in the solution. The generated precursor droplets were subjected to pyrolysis within a vertical quartz reactor maintained at 700 °C, using N$_2$ as the carrier gas. During pyrolysis, the N-rich species present in PVP decomposed into an N-doped AC matrix, whereas Fe$_2$O$_3$ nanoparticles were formed due to the presence of O-containing nitrate (NO$_3^-$) anion groups in the precursor salt and carboxyl groups in PVP, despite the inert atmosphere. This process resulted in the formation of microspheres containing Si and Fe$_2$O$_3$ nanoparticles uniformly embedded within an AC matrix, referred to as Si/Fe$_2$O$_3$/AC microspheres (Scheme 1-②). During the initial heat treatment, Si/Fe$_2$O$_3$/AC precursor microspheres were exposed to DCDA at 800 °C under a N$_2$ atmosphere. This step resulted in the reduction of the Fe$_2$O$_3$ nanoparticles to metallic Fe nanocrystals. The surrounding PVP-derived N-doped AC matrix restricted the grain growth and aggregation of metallic Fe nanocrystals, while the matrix itself was transformed into NGC owing to the catalytic effect of the Fe nuclei. The NGC matrix served as the primary pathway for rapid electron transfer. Additionally, N-CNTs were grown on the microsphere surfaces using metallic Fe nanocrystals as catalysts, which acted as secondary conductive pathways. These N-CNTs emerged through catalytic chemical vapor deposition, utilizing CH$_x$ and NH$_3$ gases

generated from DCDA (Scheme 1-③). In the second heat treatment step, selenization was performed at 300 °C under H$_2$/Ar (vol = 5:95%) atmosphere, as shown in Scheme 1-④. Excess Se was used in a similar manner. During this step, a phase conversion from metallic Fe to FeSe$_2$ occurred in an H$_2$Se atmosphere, which was formed due to the combination of H$_2$ with Se. This process resulted in the formation of microspheres comprising biphasic Si-FeSe$_2$ nanocrystals enveloped within an NGC–AC matrix along with well-grown N-CNTs, referred to as Si/FeSe$_2$@NGC–AC/N-CNT microspheres. In the final step, a third heat treatment was carried out at 300 °C under air atmosphere (Scheme 1-⑤). During the oxidation process, the FeSe$_2$ phase transformed into an amorphous FeSeO$_x$ phase. This phase change characterizes a kinetically favored redox reaction owing to fast Li-ion diffusion and high structural integrity.[30] Simultaneously, AC was selectively removed from the carbon matrix, creating micropores that enhanced the overall electrochemical performance. The porous structure not only facilitated efficient electrolyte infiltration, but also mitigated undesirable volume expansion.

A comprehensive analysis was conducted to characterize the nanostructures obtained at various stages of the synthesis and to elucidate the formation mechanism. Figure S1, Supporting Information, shows the physical characterization of the commercial Si nanopowder employed in the spray solution. The field-emission scanning electron microscopy (FE-SEM) image in

**ADVANCED
SCIENCE NEWS**

www.advancedsciencenews.com

**small
structures**

www.small-structures.com

Figure S1a, Supporting Information, shows the spherical Si nanoparticles with diameters ranging from 40 to 120 nm. The X-ray diffraction (XRD) pattern of the nanopowder (Figure S1b, Supporting Information) exhibits three distinct diffraction peaks at $2\theta = 28$, 47, and 56°, corresponding to the (111), (022), and (311) crystallographic planes, respectively, and are indicative of the presence of pure Si. Furthermore, Figure S2, Supporting Information, provides insights into the morphology and crystal structure of the as-prepared microspheres obtained after spray pyrolysis. The FE-SEM image (Figure S2a, Supporting Information) shows the uniform formation of nonaggregated microspheres with an average diameter of ≈1.5 μm. Closer examination using a high-magnification FE-SEM image (Figure S2b, Supporting Information) revealed that all the constituents were well confined within the microsphere. In addition, the rough surface of the microspheres was also apparent, which was attributed to the presence of Si nanoparticles. Additionally, a fractured surface view of the microspheres (Figure S2c, Supporting Information) confirmed the uniform distribution of nanosized Si particles within the internal structure. The XRD pattern (Figure S2d, Supporting Information) shows distinct high-intensity peaks at the same positions as those observed for pure Si (Figure S1b, Supporting Information), confirming the presence of Si in the as-sprayed powder. Furthermore, diffraction peaks corresponding to different Fe_2O_3 crystal phases were also observed. These peaks appear due to the reaction of Fe^{3+} cations with the O-containing species present in both the Fe salt and PVP molecules.

The as-sprayed $Si/Fe_2O_3/AC$ microspheres obtained above underwent an initial heat treatment at 800 °C for 5 h under a N_2 atmosphere in the presence of DCDA which acted as the carbon source, leading to the formation of highly densified N-CNTs that became intricately intertwined with the microspheres. The posttreatment morphological and crystal structure changes in the microspheres are depicted in **Figure 1**. The spherical morphology of the microspheres remained unaltered after the treatment, as evident from the FE-SEM image shown in Figure 1a. However, a significant transformation occurred on the surface of the microspheres, which became fully covered with well-grafted N-CNTs due to the reaction of the metallic Fe catalyst with the CH_x and NH_3 gases generated during the decomposition of DCDA. Notably, the Fe_2O_3 nanocrystals within the microspheres were reduced to metallic Fe nanoparticles via a carbo-reduction process. The magnified transmission electron microscopy (TEM) image in Figure 1b firmly indicated the presence of well-grown N-CNTs. The high-magnification TEM image in Figure 1c reveals that the formed N-CNTs have an outer diameter of ≈20–30 nm and a length of up to several hundred nanometers. Additionally, the aspect ratio of N-CNTs grown on the surface of Si/Fe@NGC–AC/N-CNT microspheres was investigated and respective ratio distribution of N-CNTs was shown in Figure S3, Supporting Information. As a result, the aspect ratio distribution of N-CNTs exhibited a Gaussian normal distribution with a ratio center of 58, with a high average aspect ratio of 75, which could facilitate a more efficient electrical network within the electrode, leading to a reduction in internal resistance. Additionally, well-implanted metallic Fe nanoparticles ($\phi = 14$ nm) inside the CNT wall (thickness of ≈2.5 nm) were apparent along with the Si nanoparticles ($\phi = 40$ nm), as

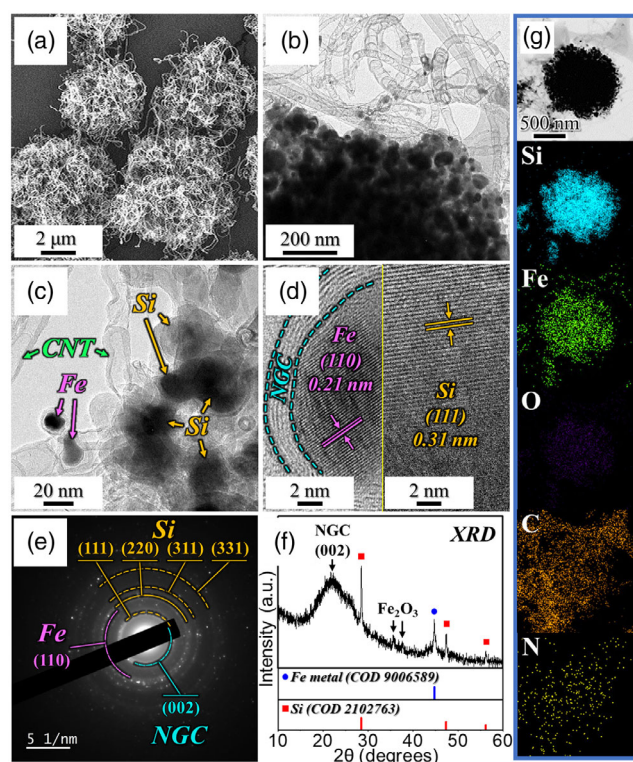**Figure 1.** Morphologies, SAED, XRD patterns, and elemental mapping images of Si/Fe@NGC–AC/N-CNT microspheres obtained after first heat treatment with DCDA at 800 °C under N_2 atmosphere: a) FE-SEM image, b,c) TEM images, d) HR-TEM images, e) SAED pattern, f) XRD pattern, and g) elemental mapping images.

evident from Figure 1c. The high-resolution TEM (HR-TEM) images in Figure 1 d reveal lattice fringes with separation of 0.21 nm corresponding to the (110) plane of the metallic Fe nanoparticles. Furthermore, an NGC layer was also observed with a lattice fringe distance of 0.34 nm, corresponding to the (002) plane of the GC surrounding the Fe nanoparticles. Lattice fringes were also found with a separation of 0.31 nm corresponding to the (111) plane of the Si nanocrystals. The NGC layer was produced by the graphitization of PVP-derived N-doped carbon species through the catalytic effect of metallic Fe. N-doping of CNTs and the GC matrix enhanced the overall electrical conductivity of the nanostructure owing to its smaller atomic radius and higher electronegativity compared with carbon.[31,32] Furthermore, the NGC layer and well-grafted N-CNTs acted as primary and secondary transport pathways, respectively, for rapid and continuous electron transfer, thereby supporting swift redox processes during the electrochemical process. Moreover, to support the above discussions, Raman and EA analysis of N-CNTs well-grafted microspheres were performed, and their characterization results were compared with Si/Fe@NGC–AC microspheres without N-CNT obtained by DCDA-free carbonization of as-prepared $Si/Fe_2O_3/AC$ microspheres (Figure S4, Supporting Information). The FE-SEM image of Si/Fe@NGC–AC microspheres displayed the spherical morphologies with no growth of N-CNTs (Figure S4a, Supporting Information). In the Raman analysis results (Figure S4b, Supporting

Information), the Si/Fe@NGC–AC/N-CNT microspheres exhibited a peak at 2685 cm^{-1} corresponding to 2D-band attributed to the overtone of the D-band,[33] while no peak was observed in the Si/Fe@NGC–AC microspheres. The 2D-band is a result of the double resonance effect related to the bonding structure of CNTs,[34] and its presence in the Raman analysis of Si/Fe@NGC–AC/N-CNT microspheres strongly suggests the successful growth of N-CNTs unlike Si/Fe@NGC–AC microspheres. Furthermore, the I_D/I_G ratio of Si/Fe@NGC–AC/N-CNT microspheres was 0.90, lower than that of Si/Fe@NGC–AC (I_D/I_G ratio = 0.95), clearly indicating the high crystallinity of the formed N-CNTs. Additionally, the N-contents in Si/Fe@NGC–AC and Si/Fe@NGC–AC/N-CNT microspheres were quantified to be 1.3 and 2.4 wt%, respectively, through the EA results (Figure S4c, Supporting Information). After standardizing the C and N-contents in Si/Fe@NGC–AC/N-CNT microspheres under the assumption that the Si and Fe-species contents in the two microspheres are identical, the N-content in Si/Fe@NGC–AC/N-CNT microspheres was 3.9 wt%, along with the N-content in the grown CNTs was calculated to be 2.6 wt%. These results support the successful formation of highly crystalline N-doped CNTs on the microsphere surface, which can serve as conductive electron transport networks supporting swift redox processes and improving the overall electrical conductivity of the nanostructure. The selected area electron diffraction (SAED) pattern in Figure 1e displays well-resolved diffraction rings of pure Si, metallic Fe, and carbonaceous materials, such as CNT and NGC, in the nanostructure, supporting the above results. Similarly, the XRD pattern in Figure 1f shows sharp diffraction peaks associated with pure Si, metallic Fe, and graphitic carbon, which are consistent with the HR-TEM and SAED results. Additionally, the mean crystallite sizes of Si and metallic Fe were calculated to be 36 and 15 nm, respectively, using the Scherrer equation by considering the high-intensity reflection of the (111) plane for Si and the (110) plane for metallic Fe. A few low-intensity diffraction peaks of Fe$_2$O$_3$ attributed to the surface oxidation of metallic Fe were also observed. The elemental mapping images in Figure 1g show the homogeneous distribution of Si, Fe, O, C, and N elements in the microspheres, confirming the formation of Si/Fe@NGC–AC/N-CNT. The trivial presence of the O element was attributed to the surface oxidation of metallic Fe nanoparticles.

The Si/Fe@NGC–AC/N-CNT microspheres obtained above were further subjected to an additional selenization process at 300 °C for 6 h under a gas mixture of H$_2$/Ar (vol = 5:95%). The corresponding microstructural and phase changes are shown in **Figure 2**. Remarkably, the overall structure of microspheres, with well-grafted N-CNTs, remained intact after the heat treatment, as evidenced by the images in Figure 2a–c. Upon closer examination using magnified TEM images in Figure 2d, metallic Fe nanoparticles (ϕ = 20 nm) inside the N-CNTs along with the Si nanoparticles (ϕ = 60 nm) were observed. Furthermore, during selenization, the FeSe$_2$ phase was successfully formed through the reaction of metallic Fe and Fe$_2$O$_3$ with H$_2$Se gas generated by the combination of H$_2$ and Se precursor. The HR-TEM image in Figure 2e reveals well-resolved lattice fringes separated by 0.19 nm corresponding to the (112) plane of the FeSe$_2$ crystal lattice. Moreover, an NGC layer surrounding the FeSe$_2$ nanoparticles is evident along with Si nanoparticles
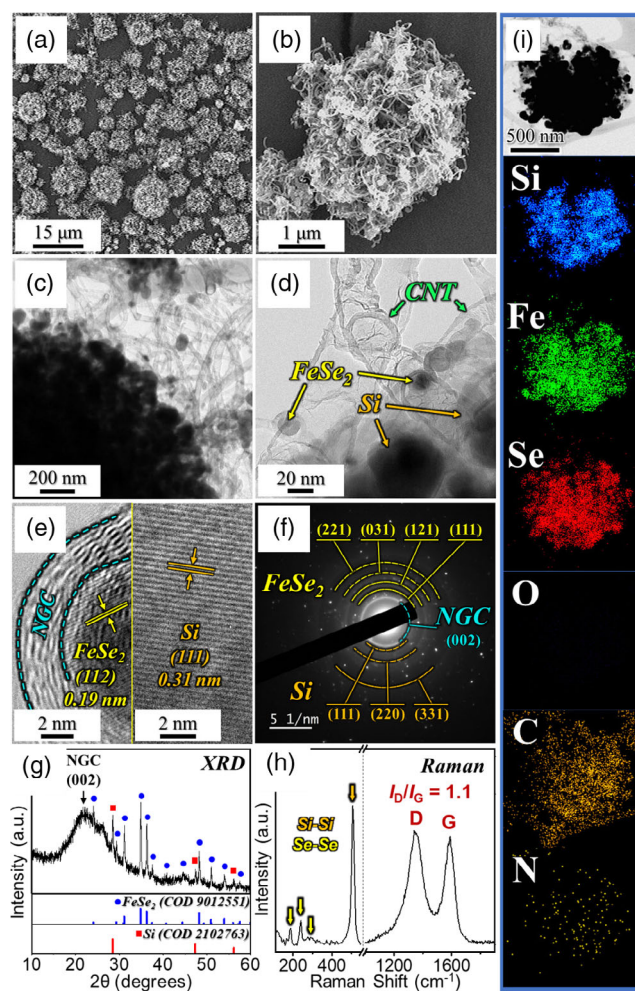

Figure 2. Morphologies, SAED, XRD patterns, Raman spectrum, and elemental mapping images of Si/FeSe$_2$@NGC–AC/N-CNT obtained after selenization at 300 °C: a,b) FE-SEM images, c,d) TEM images, e) HR-TEM image, f) SAED pattern, g) XRD pattern, h) Raman spectrum, and i) elemental mapping images.

with lattice fringes separated by 0.31 nm, corresponding to the (111) crystallographic plane. The SAED (Figure 2f) and XRD patterns (Figure 2g) exhibit the respective diffraction rings and diffraction peaks of FeSe$_2$, Si, and graphitic carbon, thus supporting the aforementioned results. Additionally, the crystallite size of FeSe$_2$ in the Si/FeSe$_2$@NGC–AC/N-CNT microspheres was calculated to be 32 nm using the Scherrer equation considering the highly intense (111) diffraction peak in the XRD pattern. Raman spectroscopy was employed to analyze the crystalline properties of the carbonaceous materials in the Si/FeSe$_2$@NGC–AC/N-CNT microspheres. The Raman spectrum (Figure 2h) reveals peaks at 187, 240, and 292 cm^{-1}, corresponding to Se—Se bonds, and a highly intense peak at 506 cm^{-1}, indicating Si—Si bonds.[35–37] Additionally, characteristic peaks at 1348 and 1586 cm^{-1} were observed, assigned to the D- and G-bands of the carbonaceous materials, respectively.[23,38,39] The relative intensity ratio of the D- and G-band (I_D/I_G) served as an indicator of the crystallinity of the carbonaceous matrix. Interestingly, a

high I_D/I_G value of 1.1 for the Si/FeSe$_2$@NGC–AC/N-CNT microspheres implies an increase in disorderedness, primarily attributed to the presence of abundant N-atom-doped sites in the carbonaceous matrix, resulting in low crystallinity of the nanostructure. Consistent with the Raman results, the elemental mapping images in Figure 2i show the uniform dispersion of Si, Fe, Se, C, and N elements in Si/FeSe$_2$@NGC–AC/N-CNT, indicating the formation of the desired selenide phase with a highly conductive N-doped carbon matrix. Furthermore, the absence of O element indicates a complete phase conversion from Fe$_2$O$_3$ to FeSe$_2$ during the selenization process, which is consistent with the XRD results in Figure 2g.

Precise temperature control for the formation of the FeSeO$_x$ phase and selective removal of AC in NGC matrix is critical for producing the Si/FeSeO$_x$@NGC/N-CNT microspheres. To determine the optimal oxidation temperature, thermogravimetric (TG) analysis of the Si/FeSe$_2$@NGC–AC/N-CNT microspheres was conducted in an air atmosphere (Figure S5,

Supporting Information). In the TG results, a weight gain was observed up to 250 °C, attributed to the phase conversion of FeSe$_2$ to FeSeO$_x$, followed by a rapid weight loss, signifying the decomposition of AC into the gaseous product. Based on this analysis, Si/FeSeO$_x$@NGC/N-CNT microspheres were synthesized through an oxidation process at 250 °C for 3 h under the air atmosphere, and the corresponding physical characterization results are presented in **Figure 3**. The FE-SEM images (Figure 3a,b) demonstrate that the spherical morphology, along with the highly intertwined N-CNTs, was preserved even after the multistep heat treatment process, including oxidation. TEM images in Figure 3c,d revealed FeSeO$_x$ nanoparticles ($\phi = 20$ nm) from the oxidation of FeSe$_2$, and these nanoparticles were located at each N-CNT, which is consistent with the previous results (Figure 1c and 2c). Furthermore, the magnified TEM image in Figure 3d manifests the presence of Si nanoparticles with an average size of 80 nm. No significant lattice fringes corresponding to FeSeO$_x$ nanoparticles were observed, suggesting
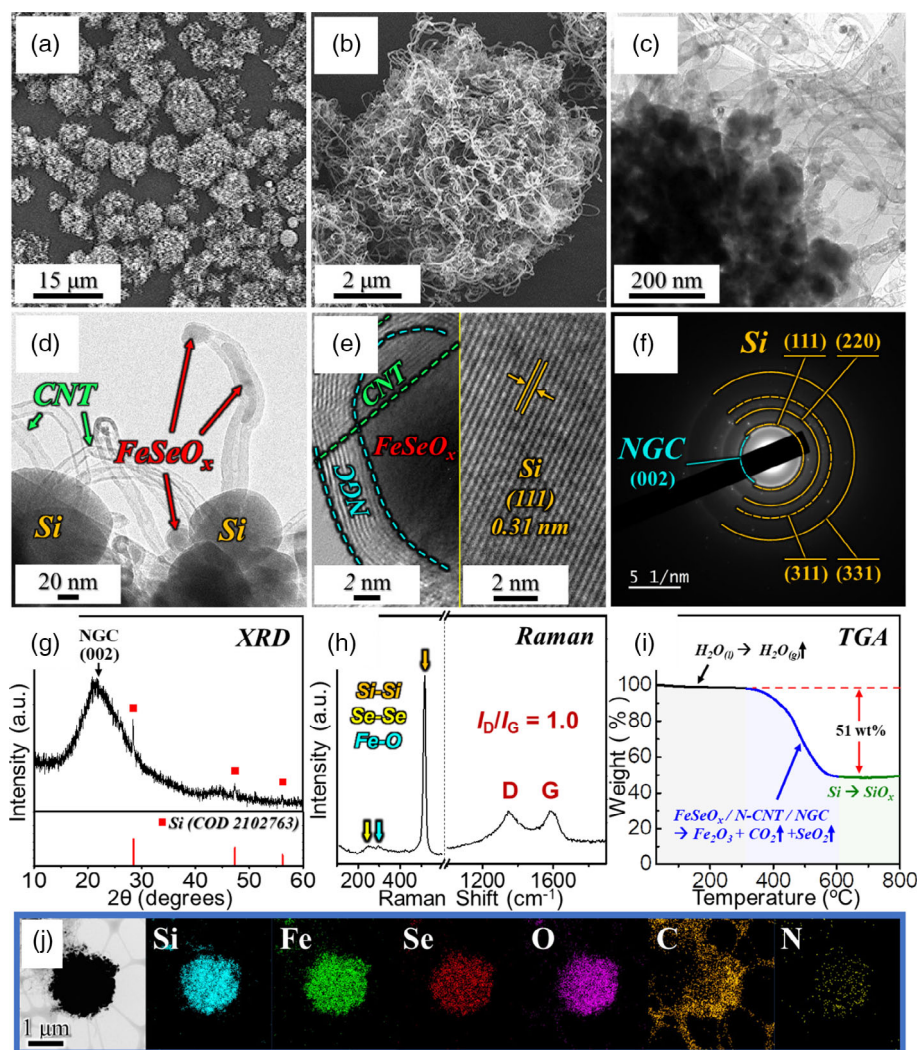

Figure 3. Morphologies, SAED, XRD patterns, Raman spectrum, TG curve, and elemental mapping images of Si/FeSeO$_x$@NGC/N-CNT obtained after oxidation at 250 °C: a,b) FE-SEM images, c,d) TEM images, e) HR-TEM image, f) SAED pattern, g) XRD pattern, h) Raman spectrum, i) TG curve, and j) elemental mapping images.

an amorphous phase. This also implies that the amorphous $FeSeO_x$ phase was formed as an intermediate between $FeSe_2$ and Fe_2O_3, as previously reported.[30,40] The HR-TEM image in Figure 3e also displays a lattice fringe spacing of 0.31 nm, corresponding to the (111) plane of Si. Besides, a lattice fringe corresponding to the NGC layer surrounding the $FeSeO_x$ nanoparticles was also evident. Corroborating this, the SAED (Figure 3f) and XRD patterns (Figure 3g) exclusively display diffraction patterns associated with Si and NGC. The XRD pattern differed from that of the $Si/FeSe_2$@NGC–AC/N-CNT microspheres (Figure 2g), primarily due to the absence of $FeSe_2$ diffraction peaks and the reduced intensity of the Si peaks, reflecting the presence of the amorphous $FeSeO_x$ phase. The existence of amorphous $FeSeO_x$ within the nanostructure was further confirmed by Raman spectroscopy (Figure 3h), which exhibited low-intensity characteristic peaks at 248 and 296 cm^{-1} corresponding to Se—Se and Fe—O bonds, respectively.[41,42] Furthermore, the prominent peaks at 518, 1344, and 1579 cm^{-1} were attributed to the Si—Si bonds of the Si nanoparticles and the D-band and G-band of the carbonaceous material, respectively.[35,38,39] The optimized oxidation process selectively removed the AC within the carbonaceous matrix, as evident from the slightly decreased I_D/I_G value of 1.0 compared to the $Si/FeSe_2$@NGC–AC/N-CNT microsphere ($I_D/I_G = 1.1$; Figure 2h). The Brunauer–Emmett–Teller (BET) surface area of the $Si/FeSeO_x$@NGC/N-CNT microsphere was measured using N_2 adsorption-desorption isotherms to validate the Raman results, as shown in Figure S6a, Supporting Information. The higher BET surface area of $Si/FeSeO_x$@NGC/N-CNT microspheres (86 $m^2 g^{-1}$) compared to that of $Si/FeSe_2$@NGC–AC/N-CNT microspheres (51 $m^2 g^{-1}$, Figure S7a, Supporting Information) resulted from the formation of micropores owing to AC combustion during oxidation. This agrees well with the pore-size distribution curve in Figure S6b, Supporting Information, and the micropore-size distribution curve in Figure S6c, Supporting Information. Additionally, mesopores (pore diameter = 40 nm) were observed in the pore-size distribution curves (Figure S6b and S7b, Supporting Information), originating from voids between the entangled N-CNTs. To further support the successful combustion of AC and formation of the $FeSeO_x$ phase, TG results for the $Si/FeSeO_x$@NGC/N-CNT microspheres were obtained (Figure 3i). The TG curve revealed weight loss up to 150 °C due to the evaporation of water within the nanostructure, followed by a plateau until 310 °C. This is not consistent with the TG results observed for the $Si/FeSe_2$@NGC–AC/N-CNT microspheres (Figure S5, Supporting Information), suggesting the formation of an amorphous $FeSeO_x$ phase during oxidation. Furthermore, the weight loss region from 310 to 610 °C ($\Delta m = -51$ wt%) was attributed to the sublimation of SeO_2, as well as the combustion of N-CNTs and the NGC matrix. The weight loss difference of ≈5 wt% between $Si/FeSeO_x$@NGC/N-CNT and $Si/FeSe_2$@NGC–AC/N-CNT microspheres ($\Delta m = -56$ wt%) is due to the absence of AC after oxidation. Furthermore, the weight increase observed at temperatures exceeding 610 °C was attributed to the gradual oxidation of Si. The elemental analysis (EA) results presented in Table S1, Supporting Information, further verify the TG results, with estimated C and N contents of 44 and 2.9 wt%, respectively, for $Si/FeSeO_x$@NGC/N-CNT microspheres. Furthermore, the

contents of Fe, Se, and Si are confirmed by wavelength dispersive X-ray fluorescence (WD-XRF) analysis, with values of 38, 26, and 36 wt% (100 wt% equivalent), respectively (Table S2, Supporting Information). Based on the EA (Table S1, Supporting Information) and WD-XRF (Table S2, Supporting Information) analysis results, the calculated contents of Si, $FeSeO_x$, and N-doped carbonaceous materials in $Si/FeSeO_x$@NGC/N-CNT microspheres are 19, 34, and 47 wt%, respectively. The elemental mapping results of the $Si/FeSeO_x$@NGC/N-CNT microspheres (Figure 3j) demonstrated a homogeneous distribution of Si, Fe, Se, O, C, and N elements in the structure, providing evidence for the successful formation of a Si and $FeSeO_x$ composite within an N-doped carbon matrix.

The bonding states and chemical environments of the elements within the $Si/FeSeO_x$@NGC/N-CNT microspheres were determined using X-ray photoelectron spectroscopy (XPS) to provide further evidence for $FeSeO_x$ formation. The XPS survey spectrum reveals the presence of Si 2p, Fe 2p, Se 3d, O 1s, C 1s, and N 1s (Figure S8, Supporting Information). The Si 2p core-level XPS spectrum (**Figure 4**a) exhibited well-fitted peaks corresponding to the two spin-orbital doublets, Si $2p_{3/2}$ and Si $2p_{1/2}$, at binding energies of 99.3 and 100.1 eV, respectively.[43,44] Additionally, peaks related to Si—O—C and Si—O were observed at 102.8 and 103.4 eV, attributed to the surface oxidation of Si nanopowder under ambient conditions.[43,44] The deconvoluted Fe 2p XPS spectrum (Figure 4b) reveals distinct Fe $2p_{3/2}$ and Fe $2p_{1/2}$ doublets. The peaks located at binding energies of 711.0/713.2 (Fe $2p_{3/2}$) and 724.3/727.0 eV (Fe $2p_{1/2}$) were ascribed to the Fe^{2+}/Fe^{3+} states in $FeSeO_x$.[45–47] Furthermore, the two shake-up satellite peaks of the Fe 2p signal (denoted as "Sat.") were confirmed at 720.5 and 732.3 eV corresponding to the antibonding orbitals between multiple anions (Se and O) and Fe atoms.[48,49] In the Se 3d core-level XPS spectrum (Figure 4c), four peaks associated with different bonding orbitals in $FeSeO_x$ were observed at 53.0/55.9 and 58.2/59.0 eV, corresponding to Se—Fe (Se $3d_{3/2}$/Se $3d_{5/2}$) and Se—O (Se $3d_{3/2}$/Se $3d_{5/2}$) bonds, respectively.[50,51] The O 1s XPS spectrum (Figure 4d) shows accurately resolved peaks at 530.7, 532.2, 533.3, and 534.5 eV corresponding to Fe—O—Se, Fe—O, Si—O, and C=O bonds, respectively.[52–54] The peaks at 284.5, 285.6, 288.7, and 289.4 eV in the C 1s XPS spectrum (Figure 4e) are associated with C=C, C—C/C—N, C=O, and O—C=O bonds, respectively.[48] In particular, the high-intensity peaks of the C=C and C—C/C—N bonds indicate the presence of the NGC matrix and N-CNTs formed through the catalytic influence of metallic Fe. Furthermore, the N 1s core-level XPS spectrum (Figure 4f) featured deconvoluted peaks at 398.4 (pyridinic-N), 400.8 (pyrrolic-N), 403.6 (graphitic-N), and 405.0 eV (oxidized-N), confirming the formation of N-doped carbon.[48,55] Overall, the systematic multistep process resulted in the formation of highly stable and conductive porous microspheres composed of biphasic Si/amorphous $FeSeO_x$ nanocrystals surrounded by an NGC matrix with highly intertwined N-CNTs. Furthermore, to highlight the advantages of the amorphous $FeSeO_x$ phase with its multianionic heterostructure, $Si/FeSeO_x$@NGC/N-CNT microspheres were compared to two samples sharing a similar morphology but featuring distinct crystalline phases, namely, Fe_2O_3 and $FeSe_2$. The Si/Fe_2O_3@NGC/N-CNT microspheres were synthesized through the oxidation of
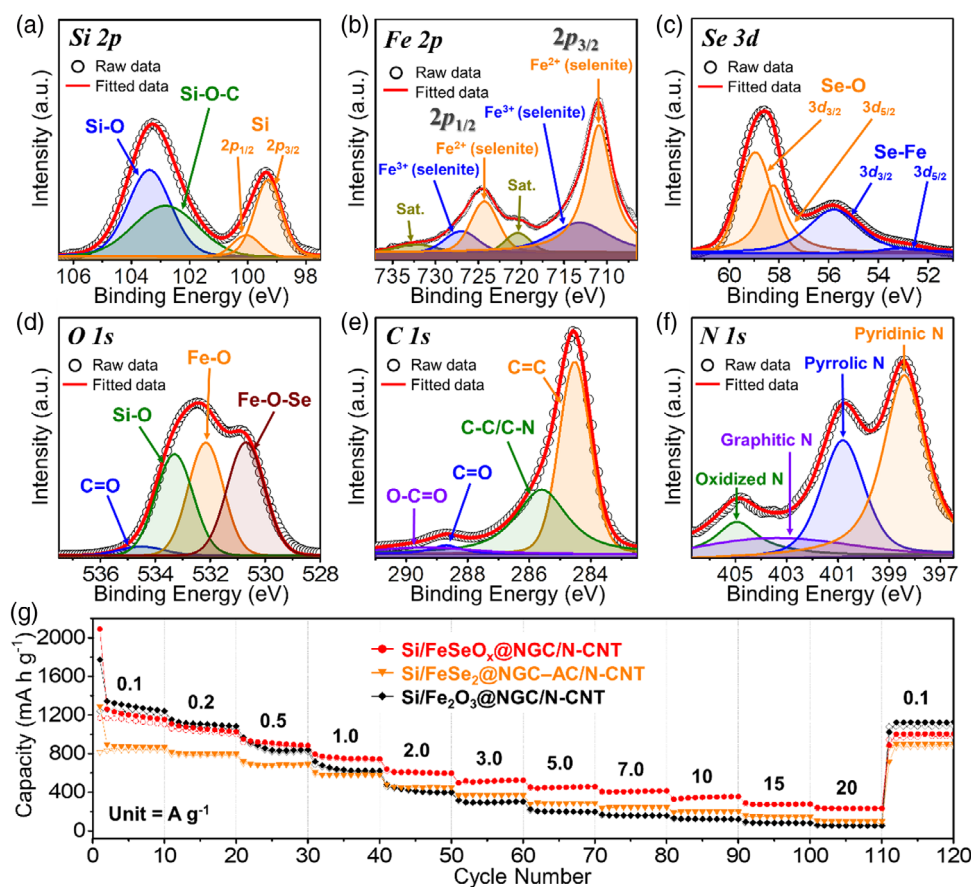
Figure 4. Core-level XPS spectra of Si/FeSeO$_x$@NGC/N-CNT and rate performances of Si/FeSeO$_x$@NGC/N-CNT, Si/FeSe$_2$@NGC–AC/N-CNT, and Si/Fe$_2$O$_3$@NGC/N-CNT microspheres: a) Si 2p, b) Fe 2p, c) Se 3d, d) O 1s, e) C 1s, f) N 1s, and g) rate performance of prepared powders with distinct crystalline phases.

Si/Fe@NGC–AC/N-CNT microspheres at 250 °C for 3 h under an ambient air atmosphere. Changes in the microstructural and crystal phases are shown in Figure S9, Supporting Information, followed by a detailed discussion. To verify the merits of the crystallographic phase of the Si/FeSeO$_x$@NGC/N-CNT microspheres, preliminary electrochemical tests (rate capabilities) were compared with those of the Si/FeSe$_2$@NGC/N-CNT and Si/Fe$_2$O$_3$@NGC/N-CNT microspheres, as shown in Figure 4g. At low current densities (below 0.2 A g^{-1}), the S @NGC/N-CNT microspheres demonstrated the highest discharge capacity owing to the high theoretical discharge capacity of Fe$_2$O$_3$ (1005 mAh g^{-1}).[56] However, the slow conversion rate of Li$_2$O formed during the conversion reaction between Fe$_2$O$_3$ and Li resulted in inferior rate performance, especially at higher current densities. In contrast, despite FeSe$_2$ having a lower theoretical discharge capacity (502 mAh g^{-1}) than Fe$_2$O$_3$, the discharge capacities of the Si/FeSe$_2$@NGC–AC/N-CNT microspheres exceeded those of the sample containing Fe$_2$O$_3$, particularly at current densities above 2.0 A g^{-1}.[57] This is due to the faster conversion rate of Li$_2$Se than that of Li$_2$O during the redox processes. Conspicuously, the amorphous FeSeO$_x$ phase is notable for its ability to enhance the electrochemical performance, which is attributed to the formation of nanoscale heterointerfaces

within the structure. This phase offers effective harnessing of both the high capacity associated with Fe$_2$O$_3$ and improved rate properties of FeSe$_2$. In line with this, the Si/FeSeO$_x$@NGC/N-CNT microspheres outperformed the other two samples in terms of discharge capacities, particularly at current densities exceeding 0.5 A g^{-1}. Even when subjected to remarkably high current densities of up to 20 A g^{-1}, the Si/FeSeO$_x$@NGC/N-CNT microspheres exhibited a remarkable discharge capacity of 233 mAh g^{-1}, highlighting their exceptional rate performance. These results firmly support the strategy of selecting the amorphous FeSeO$_x$ phase over oxide or selenide phases. Furthermore, to obtain the optimized ratio of Si and amorphous FeSeO$_x$ phase, the comprehensive physical and electrochemical characterization of the Si/FeSeO$_x$@NGC/N-CNT composites obtained after varying the ratio of Si and Fe-species to 1:3, 1:6, and 1:12 were performed, and depicted in Figure S10 and S11, Supporting Information, along with the relevant discussion.

To further assess the influence of the grafted N-CNTs and amorphous FeSeO$_x$ phases on the electrochemical performance of the Si/FeSeO$_x$@NGC/N-CNT microspheres, we synthesized microspheres composed of biphasic Si/amorphous FeSeO$_x$ composite nanocrystals surrounded by an NGC matrix without N-CNT growth (denoted as Si/FeSeO$_x$@NGC). Another sample

composed of Si nanoparticles within the AC matrix (denoted as Si/AC microspheres) was prepared for comparison. The formation mechanisms of these materials are depicted in **Figure 5**a,b. The synthesis of the Si/FeSeO$_x$/NGC microspheres, as shown in Figure 5a, involved spray pyrolysis followed by two heat treatments. The conditions during the spray solution and spray pyrolysis were identical to those for the Si/FeSeO$_x$@NGC/N-CNT microspheres. However, the powders obtained after spray pyrolysis underwent direct selenization and subsequent oxidation, skipping the N-CNT growth process. During selenization, the PVP-derived carbon matrix, which acted as a reducing agent, promoted the transformation of Fe$_2$O$_3$ into intermediate metallic Fe through a carbothermic reduction process. Subsequently, the FeSe$_2$ phase was formed by the reaction of the intermediate metallic Fe with H$_2$Se gas. During this process, the carbon matrix was graphitized using an intermediate metallic Fe catalyst. Finally, during the oxidation step, FeSe$_2$ transformed into an amorphous FeSeO$_x$ phase with the simultaneous removal of AC, resulting in the formation of Si/FeSeO$_x$@NGC

microspheres. Si/AC microspheres were also synthesized via one-pot spray pyrolysis (Figure 5b). The aqueous spray solution was prepared with PVP and Si nanopowder only, that is, without the Fe salt precursor. PVP was carbonized to AC during the spray pyrolysis process, resulting in the formation of Si/AC composite microspheres. The physical characterization results of Si/FeSeO$_x$@NGC microspheres are presented in Figure 5c–e. FE-SEM images in Figure 5c,d revealed the spherical morphology of the prepared powder (with an average size of 1.5 μm). In addition, a rough and densely packed surface was evident due to the Si nanoparticles and Fe compounds. The XRD pattern in Figure 5e indicates the presence of a distinct nanocrystalline Si phase, whereas no peaks corresponding to the FeSeO$_x$ phase were observed, confirming its amorphous nature, as discussed earlier. The Fe 2p core-level XPS spectrum (Figure S12a, Supporting Information) shows well-defined peaks corresponding to two spin-orbital doublets, Fe 2$p_{3/2}$ (711.1 eV) and Fe 2$p_{1/2}$ (724.6 eV), along with two shake-up satellite peaks for Fe.[45–47] The deconvoluted spectrum revealed well-resolved peaks at
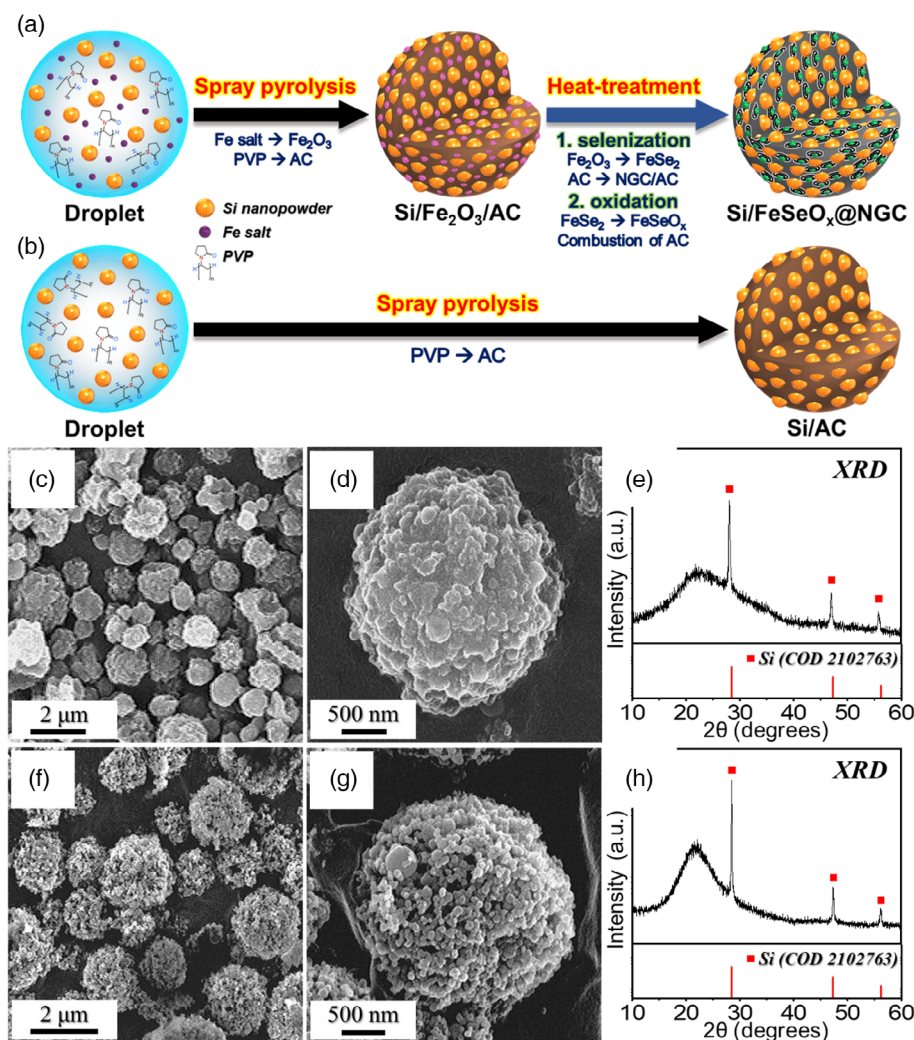

Figure 5. Schematic diagram for the formation of: a) microspheres comprising a biphasic Si/amorphous FeSeO$_x$ composite enveloped within an NGC matrix and without N-CNTs (Si/FeSeO$_x$@NGC) and b) microspheres composed of Si nanoparticles within an AC matrix (Si/AC); c,d) FE-SEM images and e) XRD pattern of Si/FeSeO$_x$@NGC microspheres; f,g) FE-SEM images and h) XRD pattern of Si/AC microspheres.

binding energies of 724.4/727.4 eV (Fe $2p_{3/2}$) and 710.9/713.3 eV (Fe $2p_{1/2}$), which were assigned to the Fe^{2+}/Fe^{3+} species in the $FeSeO_x$ phase.[45–47] The deconvoluted Se 3d XPS spectrum shown in Figure S12b, Supporting Information, exhibited four well-fitted peaks at binding energies of 53.0/55.9 for Se $3d_{3/2}$ and 58.2/59.0 eV for Se $3d_{5/2}$, which were attributed to the Se—Fe/Se—O bonds in $FeSeO_x$, respectively.[50,51] The O 1s spectrum (Figure S12c, Supporting Information) was deconvoluted into four distinct peaks at binding energies of 534.5, 533.2, 532.4, and 530.8 eV, corresponding to the C=O, Si—O, Fe—O, and Fe—O—Se species, respectively.[52–54] The Fe—O and Fe—O—Se peaks indicate the formation of the $FeSeO_x$ phase. Additionally, the appearance of Si—O peaks indicates the partial oxidation of the Si surface under atmospheric conditions. The EA result of Si/$FeSeO_x$@NGC microspheres in Table S1, Supporting Information, indicates negligible traces of carbon (1.7 wt%) compared to Si/$FeSeO_x$@NGC/N-CNT microspheres. This suggests that the carbon in the structure was mainly consumed in the carbothermic reduction of Fe species due to the absence of a reducing agent such as DCDA, along with the combustion process during the oxidation step. Moreover, the Si/$FeSeO_x$@NGC microspheres exhibited a low BET surface area of 16 $m^2\,g^{-1}$ (Figure S7c, Supporting Information) due to the absence of numerous N-CNTs throughout the structure. The Barrett–Joyner–Halenda pore-size distribution curve shown in Figure S7d, Supporting Information, suggests the presence of mesopores with a peak maximum centered at 22 nm, which can be attributed to voids between nanoparticles, such as Si and $FeSeO_x$. Similarly, physical analysis was also performed on the Si/AC microspheres, which were prepared as a comparison sample to validate the synergetic effect between amorphous $FeSeO_x$ and Si in the Si/$FeSeO_x$@NGC/N-CNT microspheres, as shown in Figure 5f–h. The FE-SEM images in Figure 5f,g depicts the spherical morphology of the prepared sample with an average diameter of 2.0 μm. The microspheres were formed due to sparsely aggregated Si nanoparticles ($\phi = 85$ nm) as primary constituent. The XRD pattern in Figure 5h reveals the coexistence of sharp and broad diffraction peaks corresponding to Si and AC, respectively. The carbon content of the Si/AC microspheres was quantified using a TG curve (Figure S13, Supporting Information). The result suggests a gradual weight loss until 550 °C due to the removal of moisture and the decomposition of AC in the microsphere. Based on the TG analysis, the estimated carbon content in the Si/AC microspheres was ≈5.9 wt%, which is consistent with the EA results (Table S1, Supporting Information).

Well-designed Si/$FeSeO_x$@NGC/N-CNT microspheres were assembled as anodes inside a CR2032 coin cell and subjected to a series of electrochemical characterizations. For a better comparison, cells utilizing Si/$FeSeO_x$@NGC and Si/AC microspheres as anodes were also prepared. Moreover, overall electrochemical results were evaluated based on the active material mass. The cyclic voltammetry (CV) curves for Si/$FeSeO_x$@NGC/N-CNT microspheres during the initial five cycles, obtained at a scan rate of 0.1 mV s^{-1} within the voltage range of 0.001 and 3.0 V, are illustrated in **Figure 6**a. In the first cathodic sweep, the weak and broad region at 2.01 V corresponds to the formation of lithium iron selenide as an intermediate, resulting from the insertion of Li-ions into amorphous iron
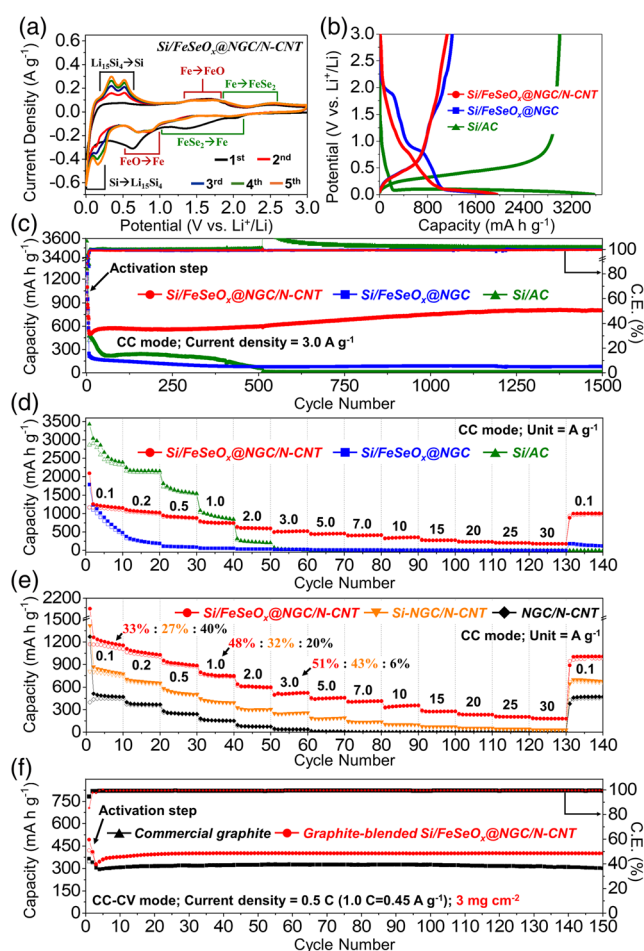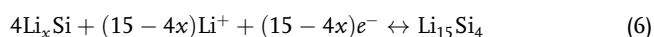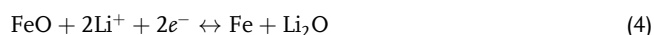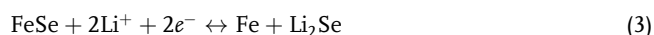

Figure 6. Electrochemical properties of Si/$FeSeO_x$@NGC/N-CNT, Si/$FeSeO_x$@NGC, and Si/AC microspheres: a) CV curves of Si/$FeSeO_x$@NGC/N-CNT for five initial cycles, b) initial discharge/charge curves for prepared microspheres at a constant current density of 0.1 A g^{-1}; c) cycling performance at a current density of 3.0 A g^{-1}; d) rate capability at various current densities ranging from 0.1 to 30 A g^{-1}, e) capacity contributions of $FeSeO_x$, Si, and NGC/N-CNT calculated by rate capabilities of Si/$FeSeO_x$@NGC/N-CNT, Si-NGC/N-CNT, and NGC/N-CNT microspheres, and f) cycling performance of graphite-blended Si/$FeSeO_x$@NGC/N-CNT and commercial graphite under the constant current–constant voltage (CC–CV) condition at 0.5 C (1.0 C = 450 mA g^{-1}).

selenide in $FeSeO_x$.[57,58] The subsequent broad peak at 1.36 V indicates the conversion of lithium iron selenide into metallic Fe and Li_2Se, accompanied by the activation of intermediate iron oxide.[56–59] The broad reduction peak at 0.63 V is attributed to the conversion reaction of iron oxide into metallic Fe and Li_2O, along with the formation of a stable SEI layer through electrolyte decomposition.[30,56,60] Additionally, the sharp peak at 0.01 V implies the formation of an amorphous $Li_{15}Si_4$ alloy phase and the insertion of Li-ions into the NGC matrix.[61–63] During the first anodic scan, the weak and broad oxidation region from 0.19 to 0.50 V indicates the phase transformation of $Li_{15}Si_4$ to amorphous Si and extraction of Li-ions from the NGC matrix.[61–63] The broad peak at 1.64 V is assigned to the

electrochemical reaction of Li_2O and metallic Fe to form the FeO phase.[56,60] The subsequent peaks at 1.87 and 2.51 V suggest the formation of FeSe intermediates from metallic Fe and Li_2Se, and the subsequent formation of $FeSe_2$ and Li-ions from FeSe intermediates, respectively.[57,58] From the second cycle onward, slightly different redox processes were observed because of the formation of an amorphous $FeO/FeSe_2$ phase, which was distinct from the amorphous $FeSeO_x$ heterointerface phase.[64] The broad peaks at 1.95 and 1.22 V indicate the conversion of $FeSe_2$ and Li-ions to form metallic Fe and Li_2Se, while the closely spaced peaks at 0.86 and 0.70 V correspond to the reaction of FeO and Li-ions.[56–58,60] The corresponding anodic peaks were also observed during the first anodic sweep. Furthermore, the broad and indistinct nature of the peaks associated with the Fe compound can be attributed to the amorphous nature of this phase. The cathodic and anodic peaks of Si at 0.16/0.01 and 0.34/0.53 V, respectively, became more distinct and their intensity increased due to the gradual activation of Si during subsequent cycles, which is consistent with previous studies.[62,63] The CV curves of $Si/FeSeO_x@NGC$ in Figure S14a, Supporting Information, exhibited similar CV characteristics with a few exceptions. For instance, the cell exhibits high-intensity redox peaks associated with the $FeSeO_x$ phase owing to the absence of CNTs. This resulted in the uncontrolled crystal growth of $FeSeO_x$ with increased insertion of Li-ions. The redox reactions involved were similar to those observed for the $Si/FeSeO_x@NGC/N-CNT$ microspheres. The complex redox reactions arising from the $FeSeO_x$ phase are firmly supported by the CV results of the $Si/FeSe_2@NGC–AC/N-CNT$ and $Si/Fe_2O_3@NGC/N-CNT$ microspheres, as shown in Figure S15, Supporting Information. Based on the above discussion, the complete reaction mechanisms involved in the discharge and charge processes of the $Si/FeSeO_x@NGC/N-CNT$ microspheres are summarized below:

For the discharge and charge process

$$FeSe_2 + xLi^+ + xe^- \leftrightarrow Li_xFeSe_2 \tag{1}$$

$$Li_xFeSe_2 + (2-x)Li^+ + (2-x)e^- \leftrightarrow FeSe + Li_2Se \tag{2}$$

$$FeSe + 2Li^+ + 2e^- \leftrightarrow Fe + Li_2Se \tag{3}$$

$$FeO + 2Li^+ + 2e^- \leftrightarrow Fe + Li_2O \tag{4}$$

$$Si + xLi^+ + xe^- \leftrightarrow Li_xSi \tag{5}$$

$$4Li_xSi + (15-4x)Li^+ + (15-4x)e^- \leftrightarrow Li_{15}Si_4 \tag{6}$$
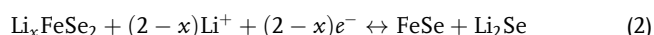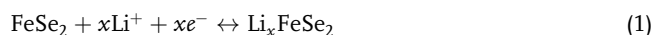
By contrast, the CV curves of the Si/AC microspheres in Figure S14b, Supporting Information, exhibited redox peaks exclusively for Si. During the initial cathodic sweep, a peak and broad region at 1.4 and 1.0–0.4 V correspond to the formation of SEI layer and the Li-insertion process of crystalline Si, respectively, leading to the formation of an amorphous Li_xSi phase.[65,66] Additionally, the cathodic peak at 0.13 V during the second cycle gradually shifted to lower voltages during subsequent cycles. This peak shift indicates a sluggish current response during cycling, resulting from the absence of CNTs and NGC matrix. To verify the CV results, initial galvanostatic discharge–charge profiles were obtained for the prepared microspheres at a current density of $0.1 A g^{-1}$, as shown in Figure 6b.

The plateaus at which the electrochemical reactions occurred were consistent with the peak positions recorded in the CV curves. For the $Si/FeSeO_x@NGC/N-CNT$ microspheres, a sloppy and ambiguous charge and discharge voltage profile was obtained, which was related to the multistep reaction of Li-ions with the amorphous $FeSeO_x$ phase at different voltage potentials. The initial discharge/charge capacities of the $Si/FeSeO_x@NGC/N-CNT$, $Si/FeSeO_x@NGC$, and Si/AC microspheres were 1954/1125, 1854/1209, and $3571/3001 mAh g^{-1}$, respectively, resulting in initial Coulombic efficiencies (ICEs) of 58, 65, and 84%, respectively. The slightly lower ICEs for $Si/FeSeO_x@NGC/N-CNT$ and $Si/FeSeO_x@NGC$ compared to those of the Si/AC microspheres are attributed to the presence of a conversion-based anode material ($FeSeO_x$ in the present case), resulting in a high initial irreversible capacity loss. Notably, FeO_x with Fe^{3+} and Fe^{2+} cation within $FeSeO_x$ is converted into metallic-Fe and Li_2O by reacting with Li-ions during the initial discharge process; however, during the charging process, the metallic Fe is converted to the FeO phase with only Fe^{2+} cation forming residual Li_2O, and the irreversible reactions result in the reduction of ICE, as reported previously.[67] Additionally, the low ICE for $Si/FeSeO_x@NGC/N-CNT$ could be attributed to the irreversible reactions forming residual Li_2O on the surface of N-CNT networks and surface side reactions, such as irreversible electrolyte degradation leading to the formation of the SEI layer, due to micropores in the structure and heterointerfaces of $FeSeO_x$.[67–69] Although the ICE for the $Si/FeSeO_x@NGC/N-CNT$ anode was low for the first cycle, it immediately increased to 96% after four cycles of activation and maintained high Coulombic efficiency (CE) values (>99%) throughout the cycling process, indicating the formation of a stable SEI layer. Furthermore, an increase in the effective C content of the structure generally leads to a relatively lower discharge capacity of the materials, and the $Si/FeSeO_x@NGC/N-CNT$ microspheres exhibit a higher carbon content of 44 wt% than the $Si/FeSeO_x@NGC$ microspheres (1.7 wt%) due to the presence of N-CNTs. Nevertheless, the almost similar or slightly higher initial discharge capacity of $Si/FeSeO_x@NGC/N-CNTs$ than that of $Si/FeSeO_x@NGC$ microspheres attests to the enhanced rate characteristics due to the N-CNTs, providing numerous conductive pathways for better charge transfer characteristics and improved diffusion kinetics. Overall, the CV and initial discharge–charge voltage profiles suggest that the structural merits induced by the coherent design strategy in the $Si/FeSeO_x@NGC/N-CNT$ microspheres enhanced Li-ion redox kinetics and improved cell performance.

To validate the CV and initial voltage profile results, the cycling and rate performances of $Si/FeSeO_x@NGC/N-CNT$, $Si/FeSeO_x@NGC$, and Si/AC microspheres were evaluated. The cycling performance of different cells featuring prepared anodes with different structural and phase characteristics was investigated at current densities of 0.5, 1.0, and $3.0 A g^{-1}$ (Figure 6c and S16, Supporting Information). Before assessing the cycling properties at $0.5 A g^{-1}$, activation steps were carried out at $0.1 A g^{-1}$ for two consecutive cycles. As observed, the $Si/FeSeO_x@NGC/N-CNT$ anode exhibited stable cycling performance until 400 cycles, delivering a reversible discharge capacity of $954 mAh g^{-1}$ with a high CE of 99.8% (Figure S16a, Supporting Information). This indicates a capacity retention of

**ADVANCED
SCIENCE NEWS**

www.advancedsciencenews.com

**small
structures**

www.small-structures.com

85% with an average decay rate of 0.038% per cycle. The excellent cycling performance of the cell with the Si/FeSeO$_x$@NGC/N-CNT anode was attributed to the synergistic effect between multiple components. For instance, after the initial discharge/charge process, FeO$_x$/FeSe$_x$ nanoparticles with heterointerfaces were formed from FeSeO$_x$ nanoparticles. Subsequently, the Si and FeO$_x$/FeSe$_x$ nanoparticles mitigated the volume expansion of each other owing to their different redox reaction voltages during the charge/discharge process, resulting in a stable cycling performance. Additionally, the NGC matrix enhanced the structural integrity of the nanostructure by restraining the volume expansion of the Si and Fe species. Although numerous strategies have been employed to mitigate volume expansion, anodes that include Si may still undergo pulverization and delamination from the Cu current collector owing to volumetric stress during the discharge/charge process. Therefore, N-CNTs were introduced onto the surface of the Si/FeSeO$_x$@NGC microspheres to prevent the fragments of the compromised structure from completely detaching, enabling stable and continuous electrochemical reactions. Comparatively, the discharge capacities of the Si/FeSeO$_x$@NGC microspheres decrease rapidly until the 50th cycle and stabilize thereafter. The sharp decrease is attributed to various factors, namely, the lowest surface area (Figure S7c, Supporting Information) resulting in sluggish Li-ion diffusion kinetics, insufficient NGC matrix (Table S1, Supporting Information) to suppress the volume expansion of electroactive materials such as Si and Fe species, and finally, absence of N-CNTs, which hinders the fast charge transfer characteristics during the redox processes. Correspondingly, the cell with Si/FeSeO$_x$@NGC anode displayed a discharge capacity of only 80 mAh g^{-1} and a CE of 99.7% at the end of 400th cycle, resulting in a capacity retention of just 8% with an average decay rate of 0.23% per cycle. Similarly, the Si/AC microspheres initially exhibited the highest capacity because of the high theoretical capacity of Si (4200 mAh g^{-1}). However, they demonstrated poor cycling performance because the microspheres lack FeSeO$_x$ nanoparticles and carbonaceous materials to accommodate the volumetric stress caused by the Si nanoparticles. Consequently, the Si/AC microsphere anode delivers a reversible capacity of 430 mAh g^{-1} at the end of 400th cycle (CE of 99.0%). The capacity retention was only 18% with an average decay rate of 0.21% per cycle. Similar capacity trends were observed at a high current density of 1.0 A g^{-1}, as shown in Figure S16b, Supporting Information. To evaluate the cycling performance at the current density of 1.0 A g^{-1}, multiple activation steps were carried out at 0.1, 0.2, and 0.5 A g^{-1} for two cycles each. At the end of 700th cycle, Si/FeSeO$_x$@NGC/N-CNT anode maintains a discharge capacity of 615 mAh g^{-1} with a CE of 99.5% and a capacity retention of 99% (with an average capacity decay rate of just 0.0021%). In contrast, Si/FeSeO$_x$@NGC and Si/AC anodes exhibit discharge capacities of 68 and 4 mAh g^{-1} with capacity retention of 15% and 0.2%, respectively, at the end of the 700th cycle. Furthermore, Si/FeSeO$_x$@NGC/N-CNT microspheres exhibit outstanding cycling performance even at a high current density of 3.0 A g^{-1} compared to Si/FeSeO$_x$@NGC and Si/AC microspheres (Figure 6c). After the activation steps at 0.1, 0.5, and 1.0 A g^{-1}, cells utilizing Si/FeSeO$_x$@NGC/N-CNT, Si/FeSeO$_x$@NGC, and Si/AC anodes exhibit reversible discharge capacities of 806, 81, and 5 mAh g^{-1}, respectively, at

the end of the 1500th cycle. As evident, the initial capacity of the Si/FeSeO$_x$@NGC/N-CNT microsphere increases for the first 50 cycles by the activation process of the electrode material, involving initially unavailable electroactive sites gradually becoming exposed and fully activated, especially at the high current density of 3.0 A g^{-1}.[70,71] Notably, the average CE of the Si/FeSeO$_x$@NGC/N-CNT microsphere up to the initial 50 cycles was calculated to be 99.1% (Figure S17, Supporting Information). The result supports the occurrence of irreversible reactions during the initial activation process, contributing to the increase in capacity. Moreover, the average CE was further improved through the graphite-blending method utilized in actual commercial processes, and the detail results are discussed later. Compared to cycling performance at 0.5 and 1.0 A g^{-1}, the Si/AC anode revealed a lower discharge capacity despite the high theoretical capacity of Si. This is due to the low intrinsic electrical conductivity of Si, resulting in poor redox kinetics especially at the high current density of 3.0 A g^{-1}. During cycling at different current densities, the Si/FeSeO$_x$@NGC/N-CNT anode showed a gradual increase in discharge capacity with repeated cycling. This is due to the expansion of the heterointerfaces within the heterostructured-FeSeO$_x$ nanocrystals and the reversible growth of a gel-like polymeric SEI film due to electrolyte degradation. As cycling progresses, a gradual expansion of the heterointerfaces in the form of the FeO$_x$/FeSe$_x$ ultrafine crystals within the FeSeO$_x$ crystal occurs, which facilitates the insertion and extraction of Li-ions during cycling, allowing for more effective utilization of the electroactive sites. Additionally, more Li-ions could be stored due to the multilayer formation effect of Li-ion at the edge sites of the heterointerfaces, resulting in a gradual increase in capacity.[72,73] Besides, the expanded heterointerface of the electroactive material induces the formation of a stable gel-like polymeric SEI film in the form of a reversible SEI layer, turning favors fast redox kinetics; hence, an increase in capacity was observed.[22,61,74] Moreover, the electrochemical characterization of the Si/FeSeO$_x$@NGC/N-CNT anodes under higher loading condition of 1.5 mg cm^{-2} were performed, and depicted in Figure S18 and S19, Supporting Information, along with the relevant discussion.

To further verify the structural merits, rate performances of the prepared microspheres were assessed at different current densities ranging from 0.1 to 30 A g^{-1}, as presented in Figure 6d. The Si/FeSeO$_x$@NGC/N-CNT microspheres exhibited discharge capacities of 1155, 1029, 885, 747, 600, 524, 459, 416, 356, 277, 233, 203, and 179 mAh g^{-1} for the 10th cycle at current densities of 0.1, 0.2, 0.5, 1.0, 2.0, 3.0, 5.0, 7.0, 10, 15, 20, 25, and 30 A g^{-1}, respectively. When the current density was reverted to 0.1 A g^{-1}, the capacity returned to 1006 mAh g^{-1} (87% retention). In contrast, cells with Si/FeSeO$_x$@NGC and Si/AC anodes exhibited inferior rate properties, with discharge capacities of 486/2390, 189/2153, 90/1552, 57/849, 33/208, and 24/8 mAh g^{-1} at current densities of 0.1, 0.2, 0.5, 1.0, 2.0, and 3.0 A g^{-1}, respectively. At current densities higher than 3.0 A g^{-1}, Si/FeSeO$_x$@NGC and Si/AC anodes showed almost zero capacities due to their structural instability and sluggish redox reaction kinetics. Furthermore, in the case of Si/AC microspheres, the capacity did not recover even after reverting the current density to 0.1 A g^{-1}, indicating the complete collapse of the structure especially at high current densities. To clarify

**ADVANCED
SCIENCE NEWS**
www.advancedsciencenews.com

**small
structures**
www.small-structures.com

the contribution for battery performance of each FeSeO$_x$, Si, and carbon components (i.e., NGC and N-CNT) in the Si/FeSeO$_x$@NGC/N-CNT anode, two-step acid treatments of microspheres were carried out using hydrochloric acid and hydrofluoric acid to selectively etch FeSeO$_x$ and Si, respectively (Figure 6e and S20, Supporting Information). The morphology, CV characteristics, and voltage profiles of the powders obtained after hydrochloric acid and hydrofluoric acid treatment were demonstrated in Figure S20a–f, Supporting Information. From the CV curves, the complete removal of FeSeO$_x$ and Si/FeSeO$_x$ in the composite was confirmed, respectively (Figure S20b,e, Supporting Information). The Si-NGC/N-CNT composite and NGC/N-CNT microspheres exhibited a reversible discharge capacity of 617, and 259 mAh g^{-1} at a current density of 1.0 A g^{-1} for the 5th cycle (Figure S20c,f, Supporting Information). As results of rate test, the capacity contributions of FeSeO$_x$, Si, and NGC/N-CNT matrix at current densities of 0.1/1.0/3.0 A g^{-1} were estimated at 33/48/51, 27/32/43, and 40/20/6%, respectively (Figure 6e). In other words, the capacity contributions of FeSeO$_x$ and Si increased with increasing current density (notably, FeSeO$_x$ increased the most), while that of the carbon matrix decreased. The reversal of the capacity contributions of Si and FeSeO$_x$, and the carbon matrix with increasing current density is attributed to the sluggish Li-ion diffusion into the carbon matrix at high current density as already reported,[75,76] as well as the promotion of rapid redox reactions of Si and FeSeO$_x$ by the N-CNT and NGC conductive frameworks serving as efficient electron transport pathways. The cycling test results at a current density of 1.0 A g^{-1} also supported the rate results, exhibiting 41, 30, and 29% capacity contribution of FeSeO$_x$, Si, and NGC/N-CNT after 200 cycles, respectively (Figure S20g, Supporting Information). Therefore, the remarkable rate capability of the Si/FeSeO$_x$@NGC/N-CNT microspheres in comparison to the Si/FeSeO$_x$@NGC and Si/AC microspheres stems from the synergetic effect of heterostructured FeSeO$_x$ and Si, followed by supporting of the highly entangled N-CNTs and NGC matrix. The heterointerface resulting from amorphous FeSeO$_x$ enhanced the redox reaction kinetics by allowing easy penetration of the electrolyte and improving the diffusion rate of Li-ions. Moreover, the microporous NGC matrix and highly entangled N-CNTs facilitate efficient and rapid charge transfer by improving the electrical contact between the active sites of FeO$_x$/FeSe$_x$ and Si nanoparticles inside the electrode. The electrochemical performance of the Si/FeSeO$_x$@NGC/N-CNT anode was better than that of other Si/carbon and Si/Fe$_x$O$_y$-based anode materials with different morphologies, as summarized in Table S3, Supporting Information.

Moreover, to evaluate the level for practical application of Si/FeSeO$_x$@NGC/N-CNT anodes, commercial graphite-blended Si/FeSeO$_x$@NGC/N-CNT anodes with a high active material loading mass of ≈3.0 mg cm^{-2} were prepared. The blend ratio of commercial graphite and Si/FeSeO$_x$@NGC/N-CNT was fixed to 10:90 weight ratio, and the electrochemical properties were evaluated under the constant current-constant voltage condition (Figure 6f and S17, Supporting Information). FE-SEM image and XRD result of commercial graphite are shown in Figure S21a,b, Supporting Information. The graphite-blended Si/FeSeO$_x$@NGC/N-CNT anode exhibited an initial discharge capacity of 420 mAh g^{-1} and an ICE of 86% at current density

of 0.1 C (1.0 C = 450 mA g^{-1}; Figure S21c, Supporting Information). As a result of the cycling test in Figure 6f, the graphite-blended Si/FeSeO$_x$@NGC/N-CNT anode showed a reversible discharge capacity of 400 mAh g^{-1} after 150 cycles at a current density of 0.5 C, which is 33% higher than that of commercial graphite (302 mAh g^{-1}). Significantly, the average CE over the initial 50 cycles of the graphite-blended Si/FeSeO$_x$@NGC/N-CNT anode was calculated to be 99.7% (Figure S17, Supporting Information), which is higher than the one before graphite-blending (99.1%), highlighting the potential of Si/FeSeO$_x$@NGC/N-CNT anode for practical application. Furthermore, all discharge capacities of graphite-blended Si/FeSeO$_x$@NGC/N-CNT anodes were much higher that of commercial graphite at various current densities from 0.1 to 5.0 C, indicating the superior rate properties of the anodes (Figure S21d, Supporting Information).

To clarify the mechanism behind the Li-ion reaction kinetics in Si/FeSeO$_x$@NGC/N-CNT, we obtained CV curves for the as-prepared samples at different sweep rates, ranging from 0.1 to 2.0 mV s^{-1}, as presented in **Figure 7**a. To distinguish between diffusion-controlled and surface-controlled reactions, the peak current (i) values obtained during the electrochemical reactions were plotted against the voltage sweep rates (v) using the following power-law equation[22,77]

$$i = av^b \tag{7}$$

$$\log(i) = b\log(v) + \log(a) \tag{8}$$

The degree to which diffusion- and capacitive-controlled processes are involved was assessed using variables a and b.[22,77] For instance, if b approaches 1.0, the redox process is predominantly capacitive- or surface-controlled, whereas if b approaches 0.5, it is diffusion controlled. The b values were calculated using the relationship between log (i) versus log (v) for peaks 1–6, which correspond to the main redox reactions and are shown in Figure 7b. The b-values for the Si/FeSeO$_x$@NGC/N-CNT anode are distinguished by the b-values related to FeSeO$_x$ (Peaks 1, 2, 5, and 6) and those related to Si (Peaks 3 and 4). The b-values for peak 1, 2, 5, and 6 related to FeSeO$_x$ in Si/FeSeO$_x$@NGC/N-CNT were 0.99, 0.92, 0.99, and 0.93, respectively, which were close to 1, suggesting the dominance of surface- or capacitive-controlled electrochemical processes. In contrast, the b-values for peaks 3 and 4 corresponding to Si were 0.72 and 0.61, indicating the both diffusion- and capacitive-controlled electrochemical processes. The reaction kinetics for Si/AC demonstrate high b values as shown in Figure S22b, Supporting Information, indicating that the redox processes are under capacitive control. Meanwhile, the reaction kinetics of the Si/FeSeO$_x$@NGC (Figure S22d, Supporting Information) displays the lowest b values, suggesting the highest proportion of diffusion-controlled processes among all samples. To quantitatively assess the contributions of the capacitive and diffusion-controlled processes, each process was isolated from the area under the total charge storage curve using the following equation[78,79]

$$i = k_1v + k_2v^{1/2} \tag{9}$$

The first term on the right-hand side (k_1v) represents the current generated by a surface-capacitive reaction, whereas the
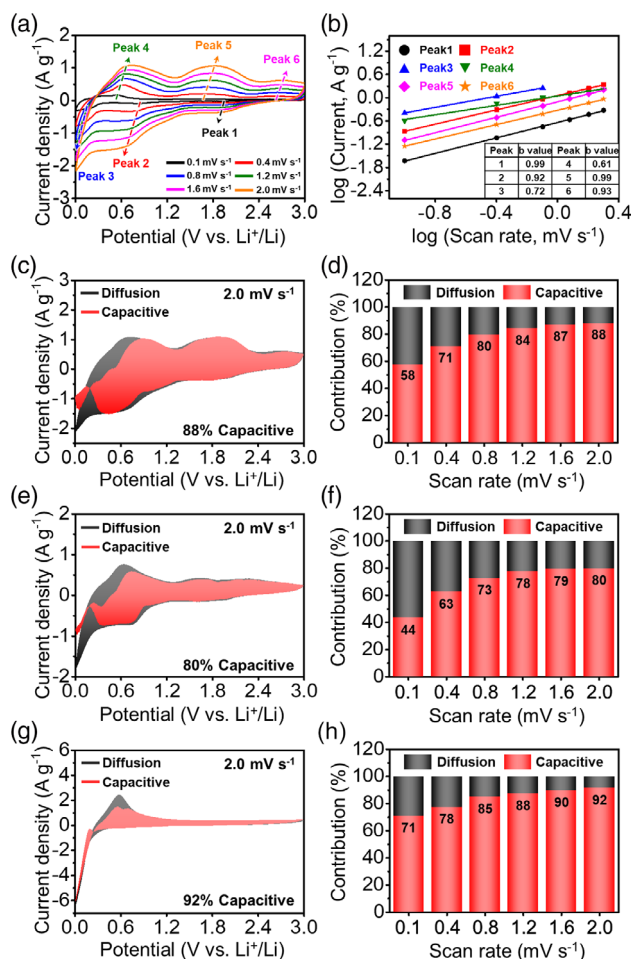
Figure 7. Electrochemical reaction dynamics analysis of a–d) Si/FeSeO$_x$@NGC/N-CNT, e,f) Si/FeSeO$_x$@NGC, and g,h) Si/AC microspheres for Li-ion storage: (a) CV curves obtained at various scan rates, (b) current response (i) versus scan rate (n) at each redox peak, c,e,g) CV curves with the capacitive fraction shown by the red region at a scan rate of 2.0 mV s^{-1}, and d,f,h) bar chart showing the percentage of the capacitive contribution at different scan rates.

second term ($k_2 v^{1/2}$) signifies the current from a diffusion-controlled reaction. The proportions of capacitive reactions relative to the total current for Si/FeSeO$_x$@NGC/N-CNT, Si/FeSeO$_x$@NGC, and Si/AC microspheres at a scan rate of 2.0 mV s^{-1} were 88, 80, and 92%, respectively (Figure 7c,e,g). The measurement of capacitive contribution at different scan rates ranging from 0.1 to 2.0 mV s^{-1} is depicted in Figure 7d,f,h. The results of Si/FeSeO$_x$@NGC/N-CNTs, Si/FeSeO$_x$@NGC, and Si/AC anodes can be attributed to the multicomponents such as Si, FeSeO$_x$, AC, NGC, and N-CNTs, which are expected to have complex interactions between them. For example, AC is characterized with capacitive-dominant reactions by Li-ion insertion through numerous defects in the structure.[80] Moreover, N-CNTs have capacitive-controlled mechanisms by limitation of Li-ion diffusion into the interior due to their closed structure, which promotes adsorption of Li-ion onto the N-sites of the N-CNT outer wall.[81] In the case of FeSeO$_x$, the

intrinsic heterointerfaces in the structure induces the capacitive-controlled reaction at the numerous interfaces, and the hetero-interface-driven mechanism further enhances the rapid surface reaction.[28,64] In contrast, Si features diffusion-controlled Li-ion storage mechanism by Li-ion diffusion within its crystal structure, followed by alloying reaction. Additionally, NGCs store Li-ion through the intercalation mechanism, which is diffusion of Li-ion into their layered structure.[82] Therefore, the higher percentage of capacitive reactions for Si/FeSeO$_x$@NGC/N-CNT (88%) compared with the Si/FeSeO$_x$@NGC microspheres (80%) can be attributed to the presence of entangled N-CNTs on the surface of the microspheres. The highly entangled N-CNTs, with their intrinsically high electrical conductivity, not only served as a secondary electronic transport pathway but also enhanced the contact between microspheres, resulting in excellent Li-ion reaction kinetics. However, Si/AC anodes exhibited a higher capacitive-controlled reaction (92%) than Si/FeSeO$_x$@NGC/N-CNT anodes, consistent with b-value fitting results (Figure S22b, Supporting Information), attributed to the structural characteristics of Si/AC microsphere despite the absence of N-CNTs and FeSeO$_x$. Briefly, the capacitive-controlled reaction of Si/AC anodes can be contributed to the loosely packed structure, as shown in the FE-SEM image (Figure 5g), and the presence of AC matrix constituting the microsphere along with the hindered diffusion-controlled reaction of Si by the absence of highly conductive NGC and N-CNTs, and heterostructured-FeSeO$_x$.

To validate the excellent Li-ion transport properties of Si/FeSeO$_x$@NGC/N-CNT microspheres, electrochemical impedance spectroscopy measurements were conducted for each sample (**Figure 8**). The Nyquist plots were obtained before and after cycling in the fully charged state. Additionally, the Nyquist plots were fitted using a deconvoluted Randle-type equivalent circuit, as shown in Figure S23, Supporting Information, and the fitted values are presented in Table S4, Supporting Information. The Nyquist plots for the fresh cells (Figure 8a) exhibited slightly higher solution resistance (R_s) values (45–47 Ω) for the Si/FeSeO$_x$@NGC and Si/AC microspheres, suggesting subtle differences in the electrode–electrolyte reaction. Furthermore, the charge transfer resistance (R_{ct}) values for Si/FeSeO$_x$@NGC/N-CNT, Si/FeSeO$_x$@NGC, and Si/AC microspheres were 199, 495, and 346 Ω, respectively (Figure 8a). The high electrical conductivities of N-CNTs and NGC contributed to the lower R_{ct} value of the Si/FeSeO$_x$@NGC/N-CNT microspheres compared with the other samples. The higher R_{ct} value of Si/FeSeO$_x$@NGC compared to that of Si/AC was due to the large crystallite size of Si/FeSeO$_x$@NGC and negligible carbonaceous material content. After the 7th cycle, the R_{ct} values for all samples decreased (Figure 8b) because of the formation of the SEI layer and the activation of Si particles after cycling, which enhanced the charge transfer kinetics. Nyquist plots of the samples after the 1300th cycle are shown in Figure 8c. The R_{ct} values of the Si/FeSeO$_x$@NGC/N-CNT, Si/FeSeO$_x$@NGC, and Si/AC microspheres were 20, 37, and 112 Ω, respectively. The presence of N-CNTs and the NGC matrix helped mitigate the stress caused by the volume expansion of the microsphere, allowing the structure to remain robust even after the 1300th cycle. The higher R_{ct} value for the Si/AC microspheres compared to the other samples was due to the structural instability of the microspheres caused by the volume expansion of the Si particles. Furthermore, the
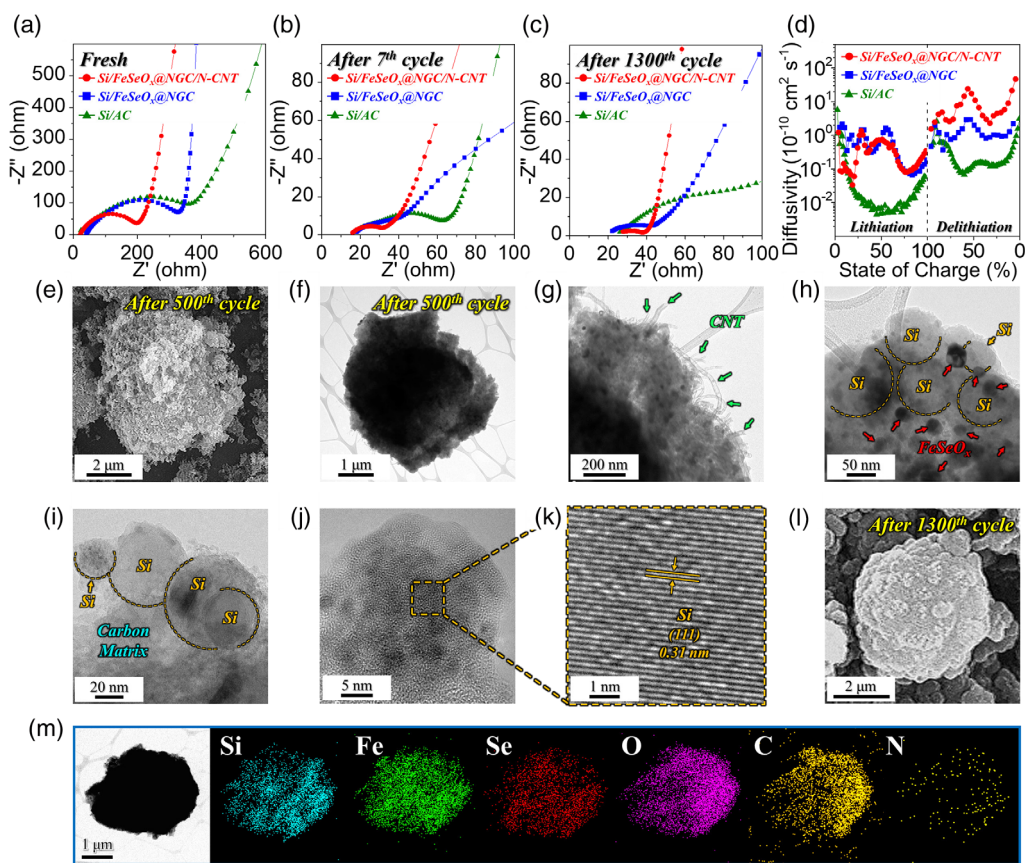
Figure 8. Nyquist impedance plots of assembled cells employed with different anodes during cycling at 3.0 A g^{-1}: a) before cycling, b) after 7th cycle, c) after 1300th cycle; d) Li-ion diffusion coefficient (D_{Li^+}) of different anodes calculated based on the GITT results versus the SoC; and FE-SEM, TEM images, and elemental dot mapping images of cycled Si/FeSeO$_x$@NGC/N-CNT electrode: e) FE-SEM image after 500th cycle, f–j) TEM images, k) HR-TEM image, l) FE-SEM image after 1300th cycle, and m) elemental mapping images of cycled Si/FeSeO$_x$@NGC/N-CNT electrode after 500th cycle.

Galvanostatic intermittent titration technique (GITT) analysis for Si/FeSeO$_x$@NGC/N-CNT, Si/FeSeO$_x$@NGC, and Si/AC anodes is conducted to provide deeper insights for the electrochemical kinetics during the lithiation/delithiation process, as shown in Figure 8d and S24, Supporting Information. Briefly, GITT analysis of the Si/FeSeO$_x$@NGC/N-CNT, Si/FeSeO$_x$@NGC, and Si/AC was measured at constant current pulse of 0.1 A g^{-1} for 30 min followed by relaxation for 2 h. Additionally, the values of Li-ion diffusion coefficient (D_{Li^+}) as a function of voltage were obtained according to the following equation[83]

$$D_{Li^+} = \frac{4}{\pi\tau}\left(\frac{m_b V_M}{M_b S}\right)^2 \left(\frac{\Delta E_s}{\Delta E_\tau}\right)^2 \left(\tau \ll \frac{L^2}{D}\right) \tag{10}$$

where τ is the current pulse time, m_b is the mass of active material, V_M is the molar volume of the active material, M_b is the molecular weight of active material, S is the geometric area of the electrode, and ΔE_s is the potential change after every equilibrium process. The determination of ΔE_s and ΔE_τ values is presented in Figure S25, Supporting Information. To clearly compare the D_{Li^+} of the three anodes calculated based on the GITT results, a graph of the D_{Li^+} of the three anodes during the lithiation/delithiation process versus state of charge (SoC) is shown in

Figure 8d, and the average D_{Li^+} values of each anode are summarized in Table S5, Supporting Information. As shown in Table S5, Supporting Information, the D_{Li^+} value for Si/FeSeO$_x$@NGC/N-CNT was calculated $\approx 3.1 \times 10^{-10}$ cm^2 s^{-1}, which is the highest compared to the Si/FeSeO$_x$@NGC (0.9×10^{-10} cm^2 s^{-1}) and Si/AC (0.3×10^{-10} cm^2 s^{-1}). The higher D_{Li^+} value recorded for Si/FeSeO$_x$@NGC/N-CNT anodes is attributed to the heterostructured FeSeO$_x$ promoting kinetically favored redox reactions and well-grown N-CNT networks acting as bridge to provide electron transport pathways between different structures thus improving diffusion kinetics in the hybrid nanostructure, as well as micropore within the structure ensuring smooth diffusion of charged species besides shortening of effective charge diffusion length. Consequently, the D_{Li^+} value for Si/FeSeO$_x$@NGC/N-CNT surpassed those of Si/FeSeO$_x$@NGC and Si/AC anodes, signifying remarkably rapid Li-ion diffusion during the initial discharge/charge cycle. Additionally, the real part of the impedance Z′ was plotted against $\omega^{-1/2}$ ($\omega = 2\pi f$ is the angular frequency) for the low-frequency region after the 1300th cycle for all samples, as shown in Figure S26, Supporting Information. The gentle slope at low frequencies for the Si/FeSeO$_x$@NGC/N-CNT microspheres demonstrates a higher Li-ion diffusion coefficient of the electrodes than that of the Si/FeSeO$_x$@NGC and Si/AC

microspheres even after 1300 cycles. The higher diffusion value for Si/FeSeO$_x$@NGC/N-CNT anodes corroborated the structural robustness of the prepared microsphere, enabling it to endure longer cycling durations while upholding the mechanical integrity of the electrode. Therefore, the excellent Li-ion reaction kinetics of Si/FeSeO$_x$@NGC/N-CNT microspheres is validated from high Li-ion diffusion coefficient value (Figure 8d) and the capacitive contribution results (Figure 7d). Moreover, the electrode thickness was measured after initial discharge, 1st cycle, and 500th cycle, and electrode thickness variation was calculated compared to fresh electrode to validate the structural benefits of Si/FeSeO$_x$@NGC/ N-CNT microspheres (Figure S27, Supporting Information). The thickness of a fresh electrode was measured as 8.3 μm (Figure S27a, Supporting Information). After the initial discharge process, the thickness of the electrode increased to 12.8 μm by lithiation of the Si/FeSeO$_x$@NGC/N-CNT anode, indicating the thickness increase rate of 54% (Figure S27b, Supporting Information). Additionally, the electrode thickness recovered to 10.9 μm after the initial cycle (31% thicker than fresh electrode), suggesting an irreversible variation during cycling (Figure S27c, Supporting Information). Accordingly, the thickness of the electrode with accumulated irreversible variation for 500 cycles was observed to increase by 98% to 16.5 μm (Figure S27d, Supporting Information). Despite the large volume expansion rate (≈360%) of Si, the electrode thickness variation of 98% after 500 cycles suggests that the volume change of Si was effectively accommodated through synergetic effect of FeSeO$_x$ with different reaction voltage with Si and NGC/N-CNT matrix. The electrode thickness swelling rate of the Si/FeSeO$_x$@NGC/N-CNT anode is comparable to those of Si-based anodes studied previously.[84–86] Furthermore, follow-up strategies could be conducted including the barrier coating on the Si nanoparticles,[87–89] optimization of the binder system,[90,91] advanced electrode design methodologies,[92,93] Si deposition to conductive scaffold using silane,[94,95] doping techniques,[92,96] and optimization of electrolyte for Si-based anodes[97,98] in the future. To gain deeper insights into the structural resilience, we obtained FE-SEM and TEM images (Figure 8e–m) of the cycled electrode after cycling at 3.0 A g^{-1}. At the end of 500th cycles, the FE-SEM and TEM images for the cycled Si/FeSeO$_x$@NGC/N-CNT electrode in Figure 8e,f reveal that the microspheres retained their original spherical morphology. Notably, the presence of highly entangled N-CNTs preventing the fragments of the compromised structure from completely detaching in the microsphere (highlighted) is evident from Figure 8g. In Figure 8h,i, the Si and FeSeO$_x$ nanoparticles are shown to remain within the carbon matrix without collapsing or detaching during the cycling processes, indicating that the N-CNTs and NGC matrix effectively accommodated the volume expansion. The TEM image in Figure 8j displays that the crystalline Si nanoparticles are polycrystallized and amorphized during the repeated lithiation/delithiation process, as reported in the previous literature.[99–101] The HR-TEM image of polycrystalline nanoparticles (Figure 8k) exhibits a lattice fringe spacing of 0.31 nm, corresponding to the (111) plane of Si. After 1300 continuous cycles (Figure 8l), substantial changes were observed. For instance, densely packed large crystals were observed, with no obvious N-CNTs, primarily due to the significant volume expansion of the active materials. Remarkably, the spherical shape of the microsphere still remained intact, suggesting outstanding

structural robustness. Elemental mapping of the cycled Si/FeSeO$_x$@NGC/N-CNT microspheres in Figure 8m also reveals an even distribution of Si, Fe, Se, O, C, and N elements within the nanostructures, providing evidence that Si and FeSeO$_x$ maintain electrical contact without detaching from the structure. In contrast, the FE-SEM image for Si/FeSeO$_x$@NGC cycled electrode in Figure S28a, Supporting Information, suggested partial rupturing of the spherical morphology along with the large crystal evolution, primarily due to unrestrained volume expansion. Likewise, the cycled morphology of Si/AC (Figure S28b, Supporting Information) reveals complete obliteration of the spherical morphology due to unaccounted volume expansion. These results strongly affirm the structural merits of Si/ FeSeO$_x$@NGC/N-CNT microspheres. The structural advantages not only account for high electrical conductivity within the nanostructure, which eventually supports kinetically favored redox processes, but also inhibit the volume expansion, thereby improving the overall electrochemical performance.

Overall, we have designed an advanced anode in the form of Si/FeSeO$_x$@NGC/N-CNT microspheres with high-rate properties and prolonged cycling performance, well supported by the synchronization strategy between the various components. This synergy successfully addresses the critical issues associated with the Si-based composite anodes and, therefore, could be applied for other nanostructures employed for wide range of applications.

3. Conclusion

We successfully synthesized a silicon hybrid anode material using a facile spray pyrolysis technique and multistep heat treatment. This multicomponent anode material consists of porous microspheres containing biphasic silicon-amorphous iron selenite nanocrystals enveloped within an NGC matrix and encased by well-grown highly intertwined N-doped CNTs. Comprehensive physical and electrochemical analyses revealed synergistic effects between the various components within the hybrid anode. These interactions facilitate swift charge transfer and unhindered movement of the charged species, thus supporting superior redox reaction capabilities. The amorphous metal selenite phase not only bolsters the structural integrity of the overall nanoarchitecture, but also expedites the diffusion of lithium ions, thereby promoting kinetically favored electrochemical processes. Benefited from the structural merits, Si/FeSeO$_x$@NGC/N-CNT, as a hybrid anode, exhibited outstanding electrochemical properties, including an impressive high-rate capability of up to 30 A g^{-1}, prolonged cycling stability across different current densities (0.5, 1.0, and 3.0 A g^{-1}), and improved lithium-ion diffusion characteristics. Moreover, graphite-blended Si/FeSeO$_x$@NGC/N-CNT anodes with a high active material loading mass of ≈3.0 mg cm^{-2} were evaluated the level for practical application, exhibited an initial CE of 86, and 33% higher reversible discharge capacity than that of commercial graphite. Therefore, the microstructural and electrochemical insights gained in this work are poised to chart new frontiers in the development of hybrid multicomponent anodes for diverse energy storage systems.

4. Experimental Section

Preparation of Si/FeSeO$_x$@NGC/N-CNT Microspheres: Porous microspheres comprising biphasic silicon-amorphous iron selenite (Si/FeSeO$_x$) nanocrystals enveloped within an NGC matrix with well-grown and highly intertwined N-CNTs (Si/FeSeO$_x$@NGC/N-CNT) were prepared using a facile spray pyrolysis technique and multistep heat treatment. To prepare the spray solution, polyvinylpyrrolidone (2.0 g) (PVP; DAEJUNG, M$_w$ = 40 000) and iron(II) nitrate enneahydrate (0.15 M) (Fe(NO$_3$)$_3$.9H$_2$O; KANTO CHEMICAL CO., INC., 98.5%) were dissolved in distilled water (200 mL) and stirred for 1 h. Subsequently, Si nanopowders (2.0 g) (ϕ = 40–120 nm, LIOYANG TONGRUN INFO Technology. Co., Ltd., >99%) were added to the solution and the mixture was ultrasonicated for 3 h, followed by vigorous stirring for 24 h. This solution, containing Si/Fe-salt/PVP, was then transferred to an ultrasonic nebulizer connected to a vertical quartz reactor. The nebulizer produced aqueous droplets, which were conveyed through a quartz reactor preheated at 700 °C, with N$_2$ serving as the carrier gas at a flow rate of 10 L min^{-1}. A detailed schematic of the spray pyrolysis technique is shown in Scheme S1, Supporting Information. Afterward, the powders obtained from the spray pyrolysis underwent a first heat treatment process in an N$_2$ atmosphere at 800 °C for 5 h, with a ramping rate of 5 °C min^{-1}. During this step, highly intertwined N-CNTs were grown using the as-prepared powder, which was loaded into an alumina crucible with a small alumina boat filled with dicyanodiamide (DCDA; Sigma–Aldrich, 99%) and covered with a lid. The weight ratio of the as-prepared powder to DCDA powder was maintained at 1:10. Following the first heat treatment, the resulting powder underwent a second heat treatment step for selenization at 300 °C for 6 h (heating rate of 5 °C min^{-1}) under a mixture gas of H$_2$/Ar (5:95 = vol%) to facilitate the formation of the FeSe$_2$ phase within the structure. Se powder (SAMCHUN, 99.5%) was used as the source of selenium gas during the process. Finally, the Si/FeSeO$_x$@NGC/N-CNT microspheres were obtained by a third heat treatment step involving oxidation at 250 °C for 3 h in an air atmosphere.

Preparation of Si/FeSeO$_x$@NGC and Si/AC Microspheres: For comparison, we also prepared microspheres comprising biphasic silicon-amorphous iron selenite (Si/FeSeO$_x$) nanocrystals enveloped within an NGC matrix, but without well-grown N-CNTs. These microspheres, denoted as Si/FeSeO$_x$@NGC, were synthesized using identical spray pyrolysis and heat treatment procedures. The as-prepared powder obtained after spray pyrolysis was subjected to a two-step heat treatment. The first step involved selenization, followed by oxidation under the aforementioned heating conditions. This resulted in the formation of Si/FeSeO$_x$@NGC microspheres. Additionally, microspheres composed solely of Si nanoparticles within an AC matrix (i.e., without the inclusion of amorphous FeSeO$_x$, NGC matrix, and well-grafted N-CNTs) were synthesized for a more comprehensive comparison. These microspheres, denoted as Si/AC microspheres, were produced using a one-pot spray pyrolysis process. To outline the synthesis procedure briefly, the spray solution for Si/AC microspheres was prepared by adding PVP (2.0 g) and Si nanopowders (2.0 g) to distilled water (200 mL). The mixture was ultrasonicated for 3 h, followed by vigorous stirring for 24 h. The temperature of the thermal reactor and flow rate of the N$_2$ carrier gas were maintained at 700 °C and 10 L min^{-1}, respectively. Notably, the detailed material characterization techniques along with cell assembly and electrochemical measurement information are included in the supporting information file.

Supporting Information

Supporting Information is available from the Wiley Online Library or from the author.

Conflict of Interest

The authors declare no conflict of interest.

Author Contributions

Jae Seob Lee: conceptualization: (lead); data curation: (equal); investigation: (equal); visualization: (equal); writing—original draft: (equal); writing—review & editing: (equal). **Jung Yeon Kim**: conceptualization: (equal); investigation: (equal); validation: (equal); visualization: (lead); writing—original draft: (equal). **Hyun Seon Ahn**: conceptualization: (equal); data curation: (equal); investigation: (lead); visualization: (lead); writing—original draft: (equal). **Hye Seon Ka**: conceptualization: (equal); data curation: (equal); investigation: (lead); visualization: (equal); writing—original draft: (equal). **Rakesh Saroha**: conceptualization: (equal); investigation: (lead); visualization: (lead); writing—original draft: (supporting). **Do Won Jeong**: formal analysis: (equal); validation: (supporting); visualization: (supporting). **Yun Chan Kang**: conceptualization: (lead); writing—original draft: (equal). **Dong-Won Kang**: conceptualization: (equal); funding acquisition: (equal); supervision: (equal); writing—review & editing: (lead). **Jung Sang Cho**: conceptualization: (lead); project administration: (lead); supervision: (equal); writing—original draft: (lead); writing—review & editing: (lead).

Data Availability Statement

Data sharing is not applicable to this article as no new data were created or analyzed in this study.

[1] A. Casimir, H. Zhang, O. Ogoke, J. C. Amine, J. Lu, G. Wu, *Nano Energy* **2016**, *27*, 359.

[2] R. Saroha, A. K. Panwar, A. Jain, J. Singh, *Ionics* **2017**, *23*, 2631.

[3] Y. J. Jo, N. H. Choi, J. D. Lee, *Korean J. Chem. Eng.* **2022**, *39*, 928.

[4] A. N. Preman, Y. E. Lim, S. Lee, S. Kim, I. T. Kim, S. Ahn, *Korean J. Chem. Eng.* **2023**, *40*, 2529.

[5] M. M. Thackeray, C. Wolverton, E. D. Isaacs, *Energy Environ. Sci.* **2012**, *5*, 7854.

[6] D. Ma, Z. Cao, A. Hu, *Nano-Micro Lett* **2014**, *6*, 347.

[7] J. Ryu, S. Park, D. Hong, S. Shin, *Korean J. Chem. Eng.* **2023**, *40*, 497.

[8] H. Wu, G. Chan, J. W. Choi, I. Ryu, Y. Yao, M. T. McDowell, S. W. Lee, A. Jackson, Y. Yang, L. Hu, *Nat. Nanotechnol.* **2012**, *7*, 310.

[9] M. Jo, S. Sim, J. Kim, P. Oh, Y. Son, *Electrochem. Commun.* **2022**, *140*, 107335.

[10] A. R. Park, M. G. Nam, A.-Y. Kim, K. S. Kim, M. S. A. S. Shah, J. Y. Lee, W.-J. Kim, J. K. Lee, P. J. Yoo, *J. Alloys Compd.* **2017**, *724*, 1134.

[11] C.-C. Wu, S. Brahma, C.-P. Liu, *J. Phys. Chem. C* **2022**, *127*, 169.

[12] B. Liu, Y. Jia, J. Li, H. Jiang, S. Yin, J. Xu, *J. Power Sources* **2020**, *450*, 227667.

[13] M. K. Majeed, A. Saleem, X. Ma, W. Ma, *J. Alloys Compd.* **2020**, *848*, 156590.

[14] X. Li, P. Meduri, X. Chen, W. Qi, M. H. Engelhard, W. Xu, F. Ding, J. Xiao, W. Wang, C. Wang, J.-G. Zhang, J. Liu, *J. Mater. Chem.* **2012**, *22*, 11014.

[15] N. Liu, H. Wu, M. T. McDowell, Y. Yao, C. Wang, Y. Cui, *Nano Lett.* **2012**, *12*, 3315.

[16] B. Wang, X. Li, X. Zhang, B. Luo, Y. Zhang, L. Zhi, *Adv. Mater.* **2013**, *25*, 3560.

[17] H.-S. Chang, S.-G. Ji, M. Rho, B.-M. Lee, S.-S. Kim, J.-H. Choi, *J. Electrochem. Sci. Technol.* **2022**, *13*, 339.

[18] J. Li, L. Christensen, M. Obrovac, K. Hewitt, J. Dahn, *J. Electrochem. Soc.* **2008**, *155*, A234.

[19] M.-H. Park, M. G. Kim, J. Joo, K. Kim, J. Kim, Y. Cui, J. Cho, *Nano Lett.* **2009**, *9*, 3844.

[20] Q. Si, K. Hanai, N. Imanishi, M. Kubo, A. Hirano, Y. Takeda, O. Yamamoto, *J. Power Sources* **2009**, *189*, 761.

[21] C. S. Kim, J. S. Lee, R. Saroha, Y. B. Park, Y. C. Kang, D.-W. Kang, S. M. Jeong, J. S. Cho, *J. Power Sources* **2022**, *523*, 231030.

[22] J. S. Lee, H. S. Ka, R. Saroha, Y. C. Kang, D.-W. Kang, J. S. Cho, *J. Energy Storage* **2023**, *66*, 107396.

[23] J. S. Lee, R. Saroha, J. H. Oh, C. Cho, B. Jin, D.-W. Kang, J. S. Cho, *J. Ind. Eng. Chem.* **2022**, *114*, 276.

[24] S. Fang, D. Bresser, S. Passerini, *Trans. Metal Oxides Electrochem. Energy Stor.* **2022**, *10*, 55.

[25] X. Deng, Z. Chen, Y. Cao, *Mater. Today Chem.* **2018**, *9*, 114.

[26] Q. Wang, C. Guo, J. He, S. Yang, Z. Liu, Q. Wang, *J. Alloys Compd.* **2019**, *795*, 284.

[27] G. D. Park, J. H. Hong, J. H. Choi, J. H. Lee, Y. S. Kim, Y. C. Kang, *Small* **2019**, *15*, 1901320.

[28] G. D. Park, S. J. Yang, J. H. Lee, Y. C. Kang, *Small* **2019**, *15*, 1905289.

[29] X.-X. Ji, Q.-H. Zhao, H. Chen, X.-W. Luo, Y. Shang, X.-D. Liu, *Nanomater.* **2022**, *12*, 2474.

[30] J. H. Kim, G. D. Park, Y. C. Kang, *Nanoscale* **2020**, *12*, 10790.

[31] M. S. Jo, J. S. Lee, S. Y. Jeong, J. K. Kim, Y. C. Kang, D. W. Kang, S. M. Jeong, J. S. Cho, *Small* **2020**, *16*, 2003391.

[32] Y.-L. Ding, P. Kopold, K. Hahn, P. A. Van Aken, J. Maier, Y. Yu, *Adv. Funct. Mater.* **2016**, *26*, 1112.

[33] L. Bokobza, J. Zhang, *Express Polym. Lett.* **2012**, *6*, 601.

[34] A. Jorio, R. Satio, *J. Appl. Phys.* **2021**, *129*, 021102.

[35] W. An, P. He, Z. Che, X. Xiao, E. Guo, C. Pang, X. He, J. Ren, G. Yuan, N. Du, D. Yang, D.-L. Peng, Q. Zhang, *ACS Appl. Mater. Interfaces* **2022**, *14*, 10308.

[36] Q. Pan, M. Zhang, L. Zhang, Y. Li, Y. Li, C. Tan, F. Zheng, Y. Huang, H. Wang, Q. Li, *ACS Nano* **2020**, *14*, 17683.

[37] K. Zhang, Z. Hu, X. Liu, Z. Tao, J. Chen, *Adv. Mater.* **2015**, *27*, 3305.

[38] S. M. Valappil, A. Zkria, S. Ohmagari, H. Naragino, H. Kato, T. Yoshitake, *Phys. Status Solidi A* **2023**, *220*, 2200627.

[39] K. A. Shah, F. A. Najar, T. Sharda, K. Sreenivas, *J. Taibah Univ. Sci.* **2018**, *12*, 230.

[40] L. Zhang, C. Lu, F. Ye, Z. Wu, Y. Wang, L. Jiang, L. Zhang, C. Cheng, Z. Sun, L. Hu, *Appl. Catal. B Environ.* **2021**, *284*, 119758.

[41] J. Li, G. Lu, G. Wu, D. Mao, Y. Guo, Y. Wang, Y. Guo, *RSC Adv.* **2013**, *3*, 12409.

[42] V. K. Yadav, G. Gnanamoorthy, D. Ali, S. P. Bera, A. Roy, G. Kumar, N. Choudhary, H. Kalasariya, A. Basnet, P. Velmurugan, *J. Nanomater.* **2022**, *2022*, https://doi.org/10.1155/2022/5949595.

[43] A. Kaur, P. Chahal, T. Hogan, *IEEE Electron Device Lett.* **2016**, *37*, 142.

[44] G. Zheng, Y. Xiang, L. Xu, H. Luo, B. Wang, Y. Liu, X. Han, W. Zhao, S. Chen, H. Chen, Q. Zhang, T. Zhu, Y. Yang, *Adv. Energy Mater.* **2018**, *8*, 1801718.

[45] S. Chen, X. Liang, S. Hu, X. Li, G. Zhang, S. Wang, L. Ma, C.-M. L. Wu, C. Zhi, J. A. Zapien, *Nano-Micro Lett.* **2023**, *15*, 47.

[46] J. Xu, W. Li, B. Zhang, L. Zha, W. Hao, S. Hu, J. Yang, S. Li, S. Gao, Y. Hou, *Chem. Sci.* **2021**, *13*, 203.

[47] S. H. Yang, Y. J. Lee, H. Kang, S.-K. Park, Y. C. Kang, *Nano-Micro. Lett.* **2021**, *14*, 17.

[48] J. S. Lee, R. Saroha, J. S. Cho, *Nano-Micro Lett.* **2022**, *14*, 113.

[49] S.-K. Park, Y. C. Kang, *ACS Appl. Mater. Interfaces* **2018**, *10*, 17203.

[50] N. Takenaka, A. Bouibes, Y. Yamada, M. Nagaoka, A. Yamada, *Adv. Mater.* **2021**, *33*, e2100574.

[51] Z. Yang, J. Y. Zhang, Z. Liu, Z. Li, L. Lv, X. Ao, Y. Tian, Y. Zhang, J. Jiang, C. Wang, *ACS Appl. Mater. Interfaces* **2017**, *9*, 40351.

[52] N. Dukstiene, L. Tatariskinaite, M. Andrulevicius, *Mater. Sci.* **2010**, *28*, 93.

[53] K. Uma, S.-W. Chen, B. K. Kumar, C. Jeyaprabha, T. C.-K. Yang, J.-H. Lin, *Ionics* **2020**, *27*, 397.

[54] X. Zhao, J. Zhao, Y. Sun, H. Ouyang, N. Chen, J. Ren, Y. Li, S. Chen, D. Yang, B. Xing, *J. Hazard. Mater.* **2022**, *424*, 127715.

[55] R. Saroha, Y. H. Seon, B. Jin, Y. C. Kang, D.-W. Kang, S. M. Jeong, J. S. Cho, *Chem. Eng. J.* **2022**, *446*, 137141.

[56] L. Xu, Y. Tian, T. Liu, H. Li, J. Qiu, S. Li, H. Li, S. Yuan, S. Zhang, *Green Energy Environ.* **2018**, *3*, 156.

[57] J. Bai, H. Wu, S. Wang, G. Zhang, C. Feng, *J. Electron. Mater.* **2019**, *48*, 5933.

[58] F. Kong. L. Lv, Y. Gu, S. Tao, X. Jiang, B. Qian, L. Gao, *J. Mater. Sci.* **2018**, *54*, 4225.

[59] Z. Zheng, P. Li, J. Huang, H. Liu, Y. Zao, Z. Hu, L. Zhang, H. Chen, M.-S. Wang, D.-L. Peng, Q. Zhang, *J. Energy. Chem.* **2020**, *41*, 126.

[60] W.-C. Shi, Y.-R. Shao, Y. Shen, Z.-F. Li, T.-L. Hu, *Mater. Lett.* **2022**, *321*, 132454.

[61] J. S. Lee, M. S. Jo, R. Saroha, D. S. Jung, Y. H. Seon, J. S. Lee, Y. C. Kang, D.-W. Kang, J. S. Cho, *Small* **2020**, *16*, e2002213.

[62] Y. Tao, Y. Tian, Y. An, C. Wei, Y. Li, Q. Zhang, J. Feng, *Sustain. Mater. Technol.* **2021**, *27*, e00238.

[63] S. H. Yang, J. K. Kim, D.-S. Jung, Y. C. Kang, *Appl. Surf. Sci.* **2022**, *606*, 154799.

[64] G. D. Park, J.-K. Lee, Y. C. Kang, *Chem. Eng. J.* **2020**, *389*, 124350.

[65] J. Liu, P. Kopold, P. A. van Aken, J. Maier, Y. Yu, *Angew. Chem. Int. Ed.* **2015**, *54*, 9632.

[66] J. Liu, Q. Zhang, T. Zhang, J.-T. Li, L. Huang, S.-G. Sun, *Adv. Funct. Mater.* **2015**, *25*, 3599.

[67] Q. Su, D. Xie, J. Zhang, G. Du, B. Xu, *ACS Nano* **2013**, *7*, 9115.

[68] M. Piwko, T. Kuntze, S. Winkle, S. Straach, P. Härtel, H. Althues, S. Kaskel, *J. Power Sources* **2017**, *351*, 183.

[69] N. Nitta, F. Wu, J. Lee, G. Yushin, *Mater. Today* **2015**, *18*, 252.

[70] Y. Luo, X. Li, Y. Zhang, L. Ge, H. Chen, L. Guo, *Electrochim. Acta* **2019**, *294*, 217.

[71] M. Liu, X. Deng, Y. Ma, W. Xie, X. Hou, Y. Fu, D. He, *Adv. Mater. Interfaces* **2017**, *4*, 1700553.

[72] Q. H. Nguyen, H. Kim, I. T. Kim, W. Choi, J. Hur, *Chem. Eng. J.* **2020**, *382*, 122981.

[73] H. Liu, Z. Huang, G. Wu, Y. Wu, G. Yuan, C. He, X. Qi, J. Zhong, *J. Mater. Chem. A* **2018**, *6*, 17040.

[74] Z.-S. Wu, W. Ren, L. Wen, L. Gao, J. Zhao, Z. Chen, G. Zhou, F. Li, H.-M. Cheng, *ACS Nano* **2010**, *4*, 3187.

[75] J. H. Park, H. Yoon, Y. Cho, C.-Y. Yoo, *Mater.* **2021**, *14*, 4683.

[76] S. Weng, G. Yang, S. Zhang, X. Liu, X. Zhang, Z. Liu, M. Cao, M. N. Ates, Y. Li, L. Chen, Z. Wang, X. Wang, *Nano-Micro Lett.* **2023**, *15*, 215.

[77] J. S. Lee, J.-S. Park, K. W. Baek, R. Saroha, S. H. Yang, Y. C. Kang, J. S. Cho, *Chem. Eng. J.* **2023**, *456*, 141118.

[78] J. S. Lee, R. Saroha, S. H. Oh, D. H. Shin, S. M. Jeong, J.-K. Kim, J. S. Cho, *Small Methods* **2021**, *5*, e2100195.

[79] L.-B. Tang, B. Zhang, C.-S. An, H. Li, B. Xiao, J.-H. Li, Z.-J. He, J.-C. Zheng, *Inorg. Chem.* **2019**, *58*, 8169.

[80] X. Wang, L. Liu, Z. Niu, *Mater. Chem. Front.* **2019**, *3*, 1265.

[81] L. Kong, Y. Zhu, P. J. Williams, M. Kabbani, F. R. Brushett, J. L. M. Rupp, *J. Mater. Chem. A* **2024**, *12*, 4299.

[82] J. Bian, M. Zheng, Q. Chen, H. Liu, *New J. Chem.* **2022**, *46*, 9372.

[83] X. Liu, R. Wang, S. Liu, J. Pu, H. Xie, M. Wu, D. Liu, Y. Li, J. Liu, *Adv. Energy Mater.* **2023**, *13*, 2302987.

[84] F. Dou, Y. Weng, Q. Wang, G. Chen, H. Liu, L. Shi, D. Zhang, *Chem. Eng. J.* **2021**, *417*, 128122.

[85] X. Li, P. Yan, X. Xiao, J. H. Woo, C. Wang, J. Liu, J.-G. Zhang, *Energy Environ. Sci.* **2017**, *10*, 1427.

[86] M. Cabello, E. Gucciardi, A. Herrán, D. Carriazo, A. Villaverde, T. Rojo, *Molecules* **2020**, *25*, 2494.

[87] K. Xu, X. Liu, K. Guan, Y. Yu, W. Lei, S. Zhang, Q. Jia, H. Zhang, *ChemSusChem* **2021**, *14*, 3981.

[88] L. Cheng, Z. Wang, T. Wang, Y. Wu, X. Liu, Y. Zhang, *J. Electroanal. Chem.* **2024**, *973*, 118670.

[89] T. Wang, H. Li, Z. Wang, L. Cheng, Y. Wu, X. Liu, L. Meng, Y. Zhang, S. Jiang, *Carbon* **2024**, *230*, 119615.

[90] Y.-G. Lee, M.-J. Lee, S.-H. Moon, S.-M. Park, *Materials* **2023**, *16*, 4266.

[91] B. Yang, T. Zhou, Y. Guo, J. Liu, *Front. Chem.* **2021**, *9*, 712225.

[92] M. K. Majeed, R. Iqbal, A. Hussain, M. U. Majeed, M. Z. Ashfaq, M. Ahmad, S. Rauf, A. Saleem, *Crit. Rev. Solid State Mater. Sci.* **2024**, *49*, 221.

[93] M. Khan, S. Yan, M. Ali, F. Mahmood, Y. Zheng, G. Li, J. Liu, X. Song, Y. Wang, *Nano-Micro Lett.* **2024**, *16*, 179.

[94] D. Lv, L. Yang, R. Song, H. Yuan, J. Luan, J. Liu, W. Hu, C. Zhong, *J. Colloid Interface Sci.* **2025**, *678*, 336.

[95] Z. Han, J. F. Wild, J. J. Chen, Y. Yang, *Energy Mater. Adv.* **2024**, *5*, 0111.

[96] M. M. Ramli, A. S. Rosman, N. S. Mazlan, M. F. Ahmad, D. S. C. Halin, R. Mohamed, N. H. Osman, A. H. Reshak, *Sci. Rep.* **2021**, *11*, 20702.

[97] Y. Yang, Z. Yang, Z. Li, J. Wang, X. He, H. Zhao, *Adv. Energy Mater.* **2023**, *13*, 2302068.

[98] J. M. Kim, R. Yi, X. Cao, Y. Xu, M. Engelhard, S. Tripathi, C. Wang, J. G. Zhang, *ACS Energy Lett.* **2024**, *9*, 2318.

[99] C. Shen, M. Ge, L. Luo, X. Fang, Y. Liu, A. Zhang, J. Rong, C. Wang, C. Zhou, *Sci. Rep.* **2016**, *6*, 31334.

[100] M. Graf, C. Berg, R. Bernhard, S. Haufe, H. Pfeiffer, H. A. Gasteiger, *J. Electrochem. Soc.* **2022**, *169*, 020536.

[101] C.-M. Wang, X. Li, Z. Wang, W. Xu, J. Liu, F. Gao, L. Kovarik, J.-G. Zhang, J. Howe, D. J. Burton, Z. Liu, X. Xiao, S. Thevuthasan, D. R. Baer, *Nano Lett.* **2012**, *12*, 1624.

2400354 (19 of 19)